Luminosity functions for galaxies and quasars in the *Spitzer* Wide-area Infrared Extragalactic Legacy Survey

T. S. R. Babbedge,[1]★ M. Rowan-Robinson,[1] M. Vaccari,[1] J. A. Surace,[2]
C. J. Lonsdale,[3,4] D. L. Clements,[1] F. Fang,[2] D. Farrah,[5] A. Franceschini,[6]
E. Gonzalez-Solares,[7] E. Hatziminaoglou,[8] C. G. Lacey,[9] S. Oliver,[10] N. Onyett,[10]
I. Pérez-Fournon,[8] M. Polletta,[4] F. Pozzi,[11] G. Rodighiero,[6] D. L. Shupe,[2] B. Siana[3]
and H. E. Smith[4]

[1]*Astrophysics Group, Blackett Laboratory, Imperial College London, Prince Consort Road, London SW7 2BW*
[2]*Spitzer Science Center, MS 220–6, California Institute of Technology, Jet Propulsion Laboratory, Pasadena, CA 91125, USA*
[3]*Infrared Processing and Analysis Center, MS 100-22, California Institute of Technology, JPL, Pasadena, CA 91125, USA*
[4]*Center for Astrophysics & Space Sciences, University of California San Diego, La Jolla, CA 92093-0424, USA*
[5]*Department of Astronomy, Cornell University, Space Sciences Building, Ithaca, NY 14853, USA*
[6]*Dipartimento di Astronomia, Universita di Padova, Vicolo Osservatorio 5, I-35122 Padua, Italy*
[7]*Institute of Astronomy, University of Cambridge, Madingley Road, Cambridge CB3 0HA*
[8]*Institute de Astrofisica de Canarias, C/ Via Lactea s/n, E-38200 La Laguna, Spain*
[9]*Institute for Computational Cosmology, University of Durham, South Road, Durham DH1 3LE*
[10]*Astronomy Centre, Department of Physics & Astronomy, University of Sussex, Brighton BN1 9QH*
[11]*Dipartimento di Astronomia, Universit di Bologna, viale Berti Pichat 6, I-40127 Bologna, Italy*

ABSTRACT

We construct rest-frame luminosity functions (LFs) at 3.6, 4.5, 5.8, 8 and 24 μm over the redshift range $0 < z < 2$ for galaxies and $0 < z < 4$ for optical quasi-stellar objects (QSOs), using optical and infrared (IR) data from the *Spitzer* Wide-area Infrared Extragalactic (SWIRE) Survey. The 3.6- and 4.5-μm galaxy LFs show evidence for moderate positive luminosity evolution up to $z \sim 1.5$, consistent with the passive ageing of evolved stellar populations. Their comoving luminosity density was found to evolve passively, gradually increasing out to $z \sim 0.5$–1 but flattening, or even declining, at higher redshift. Conversely, the 24-μm galaxy LF, which is more sensitive to obscured star formation and/or active galactic nuclei (AGN) activity, undergoes strong positive evolution, with the derived IR energy density and star formation rate (SFR) density $\propto (1 + z)^\gamma$ with $\gamma = 4.5^{+0.7}_{-0.6}$ and the majority of this evolution occurring since $z \sim 1$. Optical QSOs, however, show positive luminosity evolution in all bands, out to the highest redshifts ($3 < z < 4$). Modelling as $L^* \propto (1 + z)^\gamma$ gave $\gamma = 1.3^{+0.1}_{-0.1}$ at 3.6 μm, $\gamma = 1.0^{+0.1}_{-0.1}$ at 4.5 μm and stronger evolution at the longer wavelengths (5.8, 8 and 24 μm), of $\gamma \sim 3$. Comparison of the galaxy LFs to predictions from a semi-analytic model based on cold dark matter (CDM) indicates that an initial mass function (IMF) skewed towards higher mass star formation in bursts compared to locally be preferred. As a result, the currently inferred massive SFRs in distant submm sources may require substantial downwards revision.

Key words: galaxies: evolution – galaxies: photometry – quasars: general – cosmology: observations.

1 INTRODUCTION

A landmark result in astronomy over the last two decades was the launch of *COBE* and the subsequent discovery of a strong far-

infrared (FIR) background radiation (Fixsen et al. 1998; Hauser et al. 1998). Studies of the extragalactic background suggest at least half the luminous energy generated by stars has been reprocessed into the infrared (IR) by dust (e.g. Puget et al. 1996; Lagache et al. 1999), suggesting that dust-obscured star formation was much more important at higher redshifts than locally. Space missions, such as *IRAS* and *ISO* (*Infrared Space Observatory*), have resolved this

★E-mail: thomas.babbedge@imperial.ac.uk

background into large and significant populations of IR sources–to luminous IR galaxies ($L_{IR} > 10^{11} L_{\odot}$) at $z < 1$ and to ultra-luminous IR galaxies ($L_{IR} > 10^{12} L_{\odot}$) at $z > 1$ (e.g. see Dwek et al. 1998; Barger et al. 1999; Flores et al. 1999; Chary & Elbaz 2001; Franceschini et al. 2001; Rowan-Robinson et al. 2004). These strongly evolving populations reveal that dust-shrouded activity is pivotal in understanding the formation of stars and the central black holes in galaxies. The evolution that is required by such studies is in agreement with suggestions from longer wavelengths–the luminous submm galaxies have been shown to have median redshifts >2 (Hughes et al. 1998; Scott et al. 2002; Chapman et al. 2005), indicating that significant evolution has occurred.

Complementary results come from *Hubble Space Telescope* observations, particularly when combined with *Spitzer* observations. These show that the bulk of galaxy morphologies we see locally were put into place over $0.5 < z < 3$ (Conselice et al. 2004; Papovich et al. 2005).

A combination of these results suggests that, in order to understand the mass assembly history of the stars and central black holes in galaxies, studies need to include IR observations and be made out to high redshift.

A basic tool in the study of galaxy populations is the construction of luminosity functions (LFs). These have long been used to constrain galaxy formation models and to quantify star formation rates (SFRs) and evolution (both of luminosity and number density) but have historically been focused on optical wavelengths. Given the importance of IR-based observations to galaxy evolution we, potentially, can make large strides in understanding how galaxies assemble by constructing near-, mid- and far-IR galaxy LFs, and seeing how they evolve with redshift. The shorter wavelengths tell us how evolved stellar mass builds up, whilst longer wavelengths indicate when and where the observed starbursts that are forming these stars are occurring.

To date this has been difficult since large, deep samples are required in order to trace the evolution–earlier work using *IRAS*, *ISO* or ground-based submm observations has been hampered by sensitivity, area and (for submm) identification difficulties. One overarching feature of these earlier studies has, however, been the strong evolution demonstrated by their LFs. Some of the earliest IR LFs were constructed from the *IRAS* satellite mission (e.g. Rowan-Robinson, Helou & Walker 1987 derived 25-, 60- and 100-μm LFs). Saunders et al. (1990) used *IRAS* data to derive the 60- and 40–120 μm LFs, which were found to be indicative of strong evolution such that luminosity increases with redshift, perhaps $\propto (1 + z)^{3\pm1}$. Clements, Desert & Franceschini (2001) used deep 12-μm *ISO* data with follow-up optical imaging and spectroscopy to determine the mJy 12-μm LF, finding that the excess (in comparison to the low-redshift *IRAS* results) at high luminosities (higher redshift) was compatible with rapid luminosity evolution $\propto (1 + z)^{4.5}$. More recently, Serjeant et al. (2004) used the optical–IR bandmerged European Large Area Infrared Survey (ELAIS) Final Analysis Catalogue of Rowan-Robinson et al. (2004) to calculate the ELAIS 90-μm LF, finding that, for consistency with source counts, a luminosity evolution of $(1 + z)^{3.4\pm1}$ was required – consistent with the evolution in comoving volume-averaged SFR at $z \lesssim 1$ derived from rest-frame optical and ultraviolet (UV) surveys (e.g. Sloan Digital Sky Survey; Glazebrook et al. 2003).

The launch of *Spitzer* (Werner et al. 2004) has given a powerful tool to astronomers. Its wide-area deep-mapping survey capabilities means extensive progress can be made in our understanding of galaxy assembly, allowing the construction of LFs in multiple IR bands across wide luminosity and redshift ranges. The *Spitzer* Wide-area Infrared Extragalactic (SWIRE; Lonsdale et al. 2003, 2004) Survey makes use of all seven of *Spitzer's* imaging bands (IRAC; Fazio et al. 2004: 3.6, 4.5, 5.8 and 8 μm. MIPS, Rieke et al. 2004: 24, 70 and 160 μm) and extensive ancillary data at other wavelengths across a total area of ~49 deg^2 and has detected around 2.5-million IR sources. At the shorter IRAC wavelengths the survey can provide constraints on the more evolved stellar populations, whilst at longer wavelengths it becomes increasingly sensitive to ongoing star formation. As such, SWIRE is able to investigate the evolution of the stellar mass function, SFRs and probe galaxy luminosity and density evolution. With the combination of large area and high sensitivity, it is uniquely able to provide good statistics for the characteristic IR sources out to $z > 1$ whilst detecting rare, luminous sources out to high redshift.

In this paper, the power of SWIRE, combining both IR and optical data, is used to investigate galaxy and Type 1 active galactic nuclei (AGN) LFs so that questions on their formation, evolution and relationship over a wide redshift range can be addressed.

To carry this out, the template-fitting photometric redshift method is first extended to incorporate near-IR data and then applied to band-merged 3.6–24 μm *Spitzer* data and associated optical photometry (U, g', r', i' and Z) from one SWIRE field (ELAIS-N1). The resulting photometric redshifts and best-fitting optical and IR template solutions are then used to obtain LFs and to investigate evolution with redshift.

In Section 2, the IR and optical catalogues, data calibration and bandmerging are set out. Photometric redshifts and LF calculations are outlined in Sections 3 and 4. LFs with redshift are presented at 3.6, 4.5, 5.8, 8 and 24 μm for galaxies and Type 1 AGN in Section 5, and comparisons to other work are made in Section 6. The results of fitting functional forms to these LFs, evolution with redshift, energy density and star formation history are reported in Section 7 and overall discussions and conclusions are presented in Section 8. For this work, the flat cosmological model with $H_0 = 72$ km s^{-1} Mpc^{-1} and $\Lambda = 0.70$ is used. Throughout this paper, the term 'AGN' is used to refer to all Type I AGN as determined from optical to near-IR template fits.

2 THE DATA

2.1 Infrared data

In this paper, we consider one field observed in the first stage of the SWIRE Survey. This is 6.5 deg^2 of the ELAIS-N1 field [specifically, the area in common with the Isaac Newton Telescope Wide-Field Survey (INT WFS), see Section 2.2], centred on $16^h11^m + 54^d55^m$, for which we have bandmerged 3.6-, 4.5-, 5.8-, 8- and 24-μm catalogues. Further information on the IRAC and MIPS data processing can be found in the SWIRE Data Release 2 Document (Surace et al. 2005) and in Shupe et al. (in preparation). A plot of the IRAC, MIPS and optical coverage of ELAIS-N1 is shown in Fig. 1. The depths (5σ) are approximately 3.7, 5.4, 48 and 37.8 μJy in the IRAC bands (3.6–8 μm) and around 230 μJy at 24 μm (note that this is a factor of ~2 higher than original estimates for 24 μm; Surace et al. 2005).

2.1.1 Reliability and completeness

Reliability
One of the most important sources of unreliability is bright star artefacts. The majority of artefacts associated with bright stars were eliminated from the basic SWIRE source lists by tuning
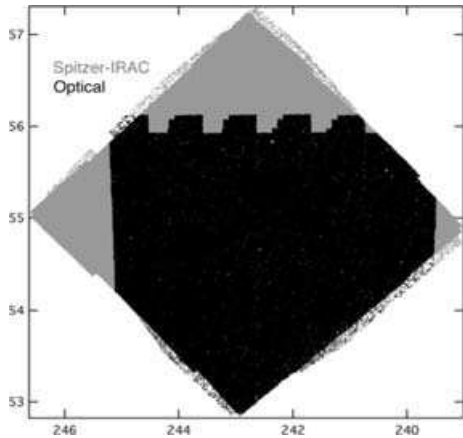
Figure 1. The *Spitzer* IRAC data (grey) and the overlap area with optical data (black). The 'crenellations' are due to the layout of the WFC CCDs. The MIPS observations are indicated by the grey dotted region, almost entirely obscured by the IRAC area. Image from Surace et al. (2005).

SExtractor to avoid their close vicinity using bespoke masks. Visual inspection of random subsets of the catalogue was carried out at all wavelengths, with results indicating a reliability >99 per cent. Investigation of the observed spectral energy distributions (SEDs) of SWIRE sources as compared to those of known objects was also carried out as a second test of reliability (Surace et al. 2005). In order to assess the reliability of the MIPS 24-μm detections, Shupe et al. (in preparation) have compared the SWIRE data with deeper guaranteed time observation (GTO) data processed using the same methods and matching extracted sources. Defining reliability as the ratio of all matched sources to all extracted SWIRE sources gives a reliability better than 98 per cent for fluxes above 0.35 mJy.

Based on studies with the bandmerged optical–IR catalogues (e.g. Rowan-Robinson et al. 2005, hereafter RR05; Surace et al. 2005), a *reliable* source is here considered to be one that has a detection with signal-to-noise ratio (S:N) > 5 in the band in question *and* a further detection in another optical or IR band. Although this approach will conceivably exclude real sources which are only detected in a single band, this is not likely to be a significant population. The largest effect might be expected for the 24-μm population–if there is a population distinct from the shorter wavelength sources then the requirement of detection in another band will introduce a bias. Of the 40 387 24-μm sources with S:N > 5, 772 have no detection at any other wavelength in the catalogue, or ∼2 per cent. Thus, any introduced bias is not severe (note that a more likely source of bias will be introduced later by requiring that the source obtains a photometric redshift).

In the area in common with the optical data (see Section 2.2), 331 209 *Spitzer* sources (81 per cent) are defined as *reliable*. Number counts are shown for each band in Fig. 2.

Completeness

The completeness of the IRAC data was evaluated by Surace et al. (2005) using a deeper field within ELAIS-N1 – the GOODS validation field (VF) (Chary et al. 2004a), taken as part of the Extragalactic First Look Survey (FLS) program. FLS and SWIRE data were compared in a 25 square arcmin area. The SWIRE 95 per cent completeness level was calculated to be at 14, 15, 42, and 56 μJy for IRAC 3.6, 4.5, 5.8 and 8 μm, respectively. A secondary analysis

via differential source counts agreed well. The overlap of 24-μm SWIRE and FLS sources was not large enough for meaningful statistics, so in order to derive the MIPS 24-μm completeness function, simulated sources were added to the central high-coverage portion of the ELAIS-N1 mosaics and SExtracted, allowing completeness versus flux to be calculated (for more details, see Shupe et al., in preparation). The completeness level at 500 μJy was calculated to be ∼97 per cent. Shupe et al. also carry out a direct estimate by comparing SWIRE data to deeper GTO data processed in the same manner, finding good agreement with the simulations for the drop in completeness with decreasing flux.

2.1.3 Bandmerging

Bandmerging of IRAC and MIPS 24-μm catalogues was carried out with the *Spitzer* Science Center's bandmerge software. Bandmerge reliability was estimated from cumulative distributions of positional offsets (Surace et al. 2005). For >90 per cent of merges, sources within 1.5 arcsec for IRAC pairs or within 3 arcsec for IRAC–MIPS-24 can be considered reliable.

2.2 Optical data

In this paper, we use optical photometry available in the ELAIS-N1 field (U, g', r', i' and Z) from the INT WFS. For more information on the survey and its goals, see McMahon et al. (2001). Basic reduction, photometry and catalogue information are outlined below.

The ELAIS-N1 ($16^h10^m + 54^d30^m$) field is approximately 9 deg^2 in U, g', r', i' and Z bands. These data have been processed at Cambridge Astronomical Survey Unit's (CASU) reduction pipeline as described in Irwin & Lewis (2001).

The mean limiting magnitudes (Vega, 5σ in 600 s) in each filter across this area are 23.40 (U), 24.94 (g'), 24.04 (r'), 23.18 (i') and 21.90 (Z), however, the completeness falls off before this, as is demonstrated by the r' magnitude distribution of sources in Fig. 2.

2.2.1 Photometric calibration and merging

Data reduction was carried out with the CASU pipeline (further details are available in Babbedge 2004 and Surace et al. 2005) with an overall photometric calibration for the survey at the level of 2 per cent. In order to merge the individual optical pointings into a single optical catalogue, an association radius of 0.9 arcsec was used (based on the seeing, 1.17 arcsec, and a nearest neighbour separation histogram). For sources that had duplicates (from overlapping tiles), the one with the lowest photometric error was retained.

2.3 Optical associations

The *Spitzer* and optical observations do not have a 100 per cent overlap. For ELAIS-N1, the area overlap is ∼70 per cent, as illustrated in Fig. 1. The optical catalogues were associated with the bandmerged SWIRE 3.6–24 μm catalogues using the WEBCMP package of IPAC's Infrared Science Archive (IRSA). WEBCMP is optimized for very fast cross-correlations, by position, between extremely large data sets. A radius of 1.5 arcsec was used for cross-identifications, a value chosen to maintain completeness whilst keeping false matches to a minimum. Where an IR source picks up multiple optical associations, the association with the highest probability indicator value, an internal WEBCMP statistic based on the match algorithm of the NASA/IPAC Extragalactic Database (NED), was retained. This match statistic
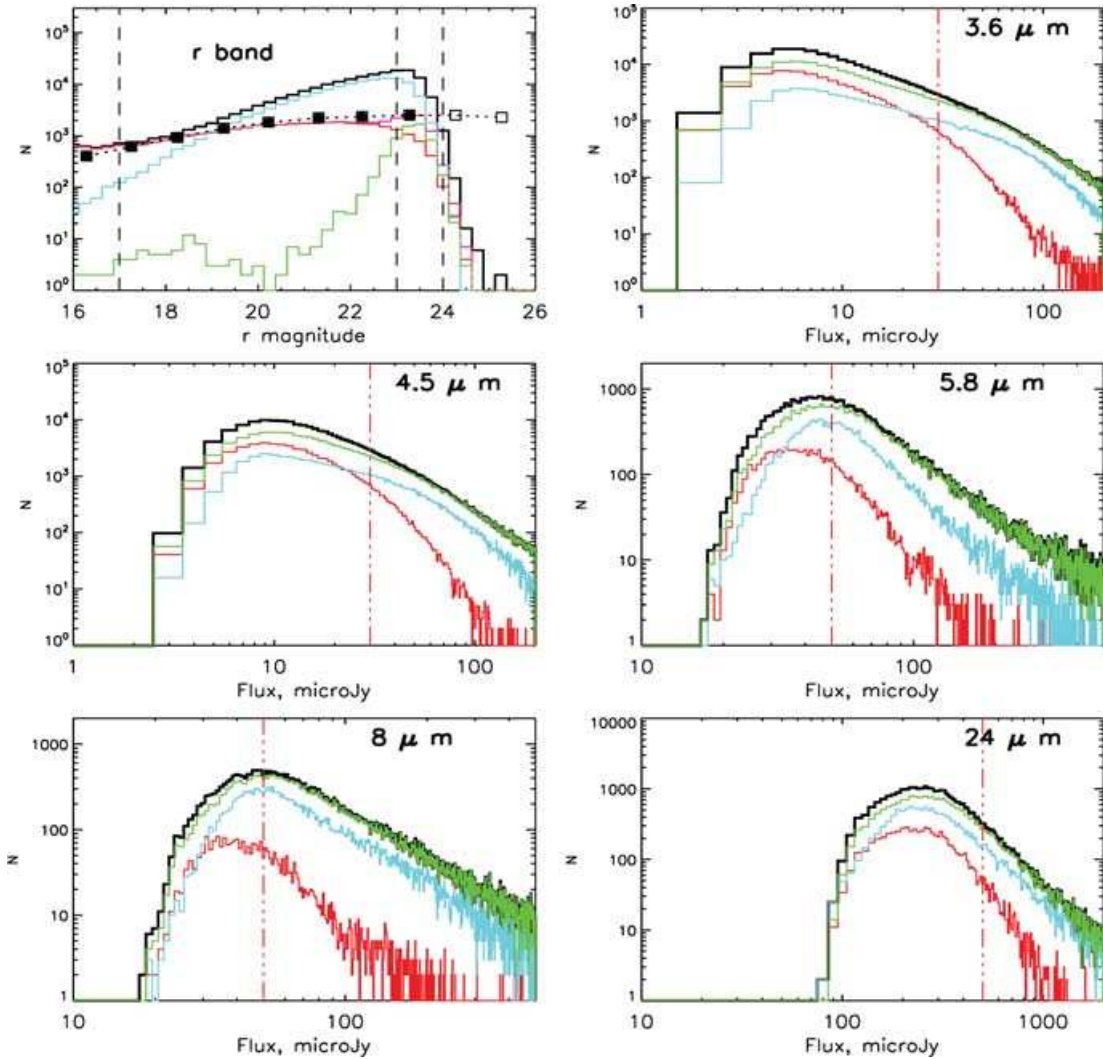
Figure 2. Number count distributions. First panel: magnitude distribution (Vega) of r'-band sources in the ELAIS-N1 full-coverage region (full optical-IRAC – MIPS overlap). *Black* histogram – all sources; *cyan* – those that obtained a photometric redshift solution; *green* – those that failed to obtain a redshift solution; *red* – those sources defined as stars and removed; *purple* – the sum of stars and photometric redshift failures. Vertical dashed lines indicate the nominal 5σ limit of 24.04 and the magnitude cuts at $r' = 23$ and 17. The filled circles joined by a dotted line represent the stellar counts from the stellar population synthesis code of Girardi et al. (2005), empty squares are where incompleteness will have a dominant effect. Remaining panels: number counts in the full-coverage region for IRAC and MIPS 24-µm sources. *Black* histogram – all reliable sources with a detection (S:N > 5) in that *Spitzer* band (will include stars); *red* histogram – the subset that are optically blank (will include stars); *green* histogram – the subset that have optical detections (will include stars); *cyan* histogram – those with a r'-band detection of $17 < r' < 23$ and which obtained a photometric redshift with $\chi^2_{red} < 10$. Vertical red dash – triple dot lines – chosen flux below which to cut sources from the LF calculations in order to maximize completeness.

is, to first order, based on the angular separation, weighted by the catalogue uncertainties.

Completeness and reliability of these *Spitzer*–optical cross-identifications (XIDs) was investigated in Surace et al. (2005) which showed that out to the maximum association radius of 1.5 arcsec, the *Spitzer*–optical XIDs are essentially 100 per cent complete, excepting the possibility of a few bright true matches at large separations. The ratio of 'false' matches to 'real' matches suggests the reliability is ~95 per cent.

Of the 331 209 reliable *Spitzer* sources in the overlap area, 82 606 are optically blank (including a small fraction in INT WFS coverage gaps), meaning 248 603 (75 per cent) of the reliable *Spitzer* sources have optical counterparts. We then make the further requirement, in order to obtain reliable photometric redshifts in Section 3.1.3, that the source be detected in four of the bands U, g', r', i', Z,

3.6 µm and 4.5 µm which reduces the sample to 180 879 sources (74 per cent).

2.4 Star/galaxy separation

Star/galaxy separation is an important but complex issue, even with the luxury of multiwavelength data. Stellarity in a band gives a measure of the compactness of a source, however, this measure is not an infallible star identifier–at faint fluxes (up to 2.5 mag above the limiting magnitude) the measure begins to break down since one can then no longer reliably differentiate between extended and point-like sources. Even at brighter fluxes, a star may not be classed as point-like in all bands (e.g. saturation effects) whilst conversely, though a nearby galaxy will be clearly extended, distant galaxies and quasars will also appear point like. Thus, effective discrimination

requires consideration of stellarity and saturation flags, magnitudes and colours.

For the identification of stars at fainter magnitudes, it is worthwhile to note that at wavelengths covered by IRAC we are well into the Rayleigh–Jeans tail of stellar blackbody curves and that stars all have essentially the same slope in their SEDs. This means that they will be colourless in the IRAC bands (in Vega magnitudes). As such, the stellar locus is well defined in colour–colour space and can be used in conjunction with stellar flags to define a robust star/galaxy separator. Here, the (3.6 µm/r') versus ($r' - i'$) diagram in conjunction with stellarity is used as the basic method to identify stars and remove them from the catalogue, as detailed in RR05. From these definitions, 41 042 of the 180 879 optical–IR sources are classed as stars (23 per cent), leaving 139 823 sources.

For the optical–IR catalogue, almost all sources with $r' < 17$ are stars, and hence for the analyses in this paper, we assume that all sources brighter than this are stars and removed. In addition, all sources that are flagged as saturated in one of more optical bands are removed, since in addition to almost certainly being stars, their photometry and stellarity designations will be unreliable. As a final cut, those sources fainter than $r' = 23$ are removed in order to maintain reliability and completeness (see Fig. 2). Thus, we are left with a catalogue of 102 645 *extragalactic* sources, with $17 < r' < 23$. These sources can now be split into extended and point-like sources, where point-like sources will be either quasars or faint galaxies. Sources are defined as point like (and so Type 1 AGN templates are considered in addition to the galaxy SEDs in photometric redshift fitting as will be described in Section 3.1) based on the optical class flags. The best bands, as found in Babbedge et al. (2004) (hereafter B04), to define stellarity are g', r' and i' so if the flag is set to 'point like' in any of these bands then the source is defined as point like. The goal here is simply to exclude those sources that do not look point like in any band from having AGN templates applied since this cuts the number of spurious high-redshift AGN fits to low-redshift galaxies. The r' magnitude distribution of sources defined as stars is compared to that of the remaining sources in Fig. 2, and it can be seen that the star distribution is relatively flat with magnitude, and dominates at the bright end. The stellar counts from the stellar population synthesis code of Girardi et al. (2005) for their *Chandra* Deep Field South (CDFS) field have been overlaid, converting from R band to r' and scaled to the same area. Both the CDFS and our ELAIS-N1 field are 'extragalactic' fields, away from the Galactic plane and bulge, so have similar proportions of each stellar population–a normal Galactic stellar population sequence (ELAIS-N1; Ibata et al. 2003). We apply an additional renormalization factor (0.74) to the total counts in the Girardi et al. model to mimic the cut placed on our multiband catalogue prior to the identification of stars. This cut was the requirement of detection in four of the bands U, g', r', i', Z, 3.6 µm and 4.5 µm, which reduced our sample by a factor of 0.74. The assumption that this same factor can be applied to the Girardi et al. counts appears reasonable since the Girardi et al. count then match our observed stellar counts at ∼$r' = 17$, where we can be confident our stellar classification is accurate. The open squares mark the approximate point at which incompleteness starts to have an effect at the faint end (based on the observed counts of Groenewegen et al. 2002 in the CDFS). This empirical comparison shows that the observed star counts distribution is in agreement with that expected from an extragalactic field. At the faint end where our ability to identify stars is less complete, some may be passed to the redshift code. However, the majority of these appear to end up in the histogram of sources that fail to obtain a redshift–comparison of the summed distribution of stars and photometric redshift failures

accounts for the majority of 'missing' stars at the faint end. It is concluded that the contamination of stars incorrectly fits as galaxies or AGN at some redshift is small.

3 TEMPLATE FITTING – A TWO-STAGE APPROACH

The emission of a galaxy at optical to near-IR and at mid-IR wavelengths is not necessarily well correlated – that is, the optical to near-IR emission will often be dominated by emission from stars, whereas at longer wavelengths reprocessed emission from dust or synchrotron emission may be the dominant contribution. Hence, for a single emission mechanism the optical to mid-IR SED of a galaxy cannot be allocated to one of a set of generic templates. Here, the analysis is separated into optical/near-IR and mid-IR, and template fitting is carried out in a two-stage approach as in RR05: optical and IRAC 3.6-, 4.5-µm detections are used for the photometric redshift fitting procedure (see Section 3.1); the longer wavelengths are then used to fit IR templates to those sources defined as having an IR excess (see Section 3.2).

3.1 Photometric redshifts and extension to IR bands

In order to calculate LFs, the redshifts of the sources are required. Here, the updated version of the IMPZ code of B04 is extended to utilize some of the IR bands from *Spitzer* and demonstrated on several sets of spectroscopic redshifts (Section 3.1.2). We seek to demonstrate both the validity and improvement gained by extending the template-fitting photometric redshift technique to incorporate near-IR data, prior to applying it to the full ELAIS-N1 optical–*Spitzer* catalogue. A more in-depth study of the photometric redshift technique, its extension to IR and application to a number of large spectroscopic samples will be presented in future work (Rowan-Robinson et al., in preparation; Andreon et al., in preparation).

An important requirement for photometric redshift fitting is that the photometry in each band is measured in the same way – different aperture sizes will sample the galaxy out to different radii, and possibly in different locations. When only using optical data, use of fixed aperture fluxes is sufficient, however, if we include IRAC near-IR fluxes it is important to be comparing like with like, and these fluxes are integrated fluxes. Hence, here for the optical bands, the aperture magnitudes corrected to the integrated magnitudes via curve-of-growth analysis are used. This procedure could introduce errors for galaxies whose integrated SEDs differ largely from the SEDs of their central regions, but in practice the results are consistent, as found in Section 3.1.2.

3.1.1 Photometric redshift method

Improvements to the code include an iteratively calculated correction to the calibration in each band (suggested by Ilbert et al. 2006) and a parabolic interpolation of the redshift solution space to improve the precision, along with improvements based on studies in RR05. One issue raised by RR05 was that for some AGN there is a significant dust torus contribution to emission at 3.6 and 4.5 µm which is problematic if the code attempts to fit it as stellar emission. One important change of the IMPZ implementation to the SWIRE data is to carry out a double pass of the code on the data, in order to deal with AGN dust tori successfully: in the first pass, the 3.6- and 4.5-µm data are not included in the fit if $S(3.6)/S(r') > 3$; in the second pass, the 3.6- and 4.5-µm data are included in the fit provided $S(3.6)/S(r') < 300$, except when the mid-IR fitting resulted in
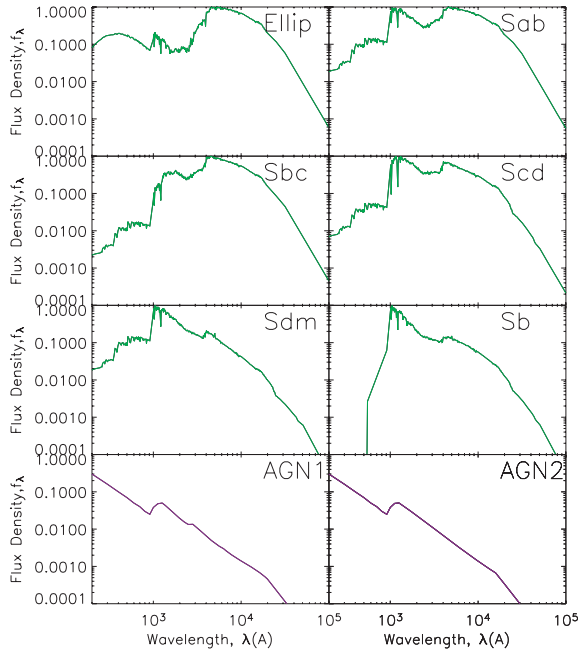
Figure 3. The templates used by IMPZ, showing the galaxy templates in green (E, Sab, Sbc, Scd, Sdm and Sb galaxies) and the two AGN templates in purple.

an AGN dust torus fit. Mid-IR excess will instead be fit separately by more appropriate SEDs – see Section 3.2.

The chosen IMPZ code setup parameters were as follows.
Templates. The six galaxy templates and two (Type 1) AGN templates of B04 are shown in Fig. 3. The two AGN templates only differ from one another at ∼3000 Å where one has a 'small blue bump' in its emission (blend of Balmer continuum and Fe II; Maoz et al. 1993). Determining the exact shape of the rest-frame far-ultraviolet (FUV) spectra of AGN is problematic. Here, a simple continuation of the power law is adopted, though at redshifts where this region enters the optical filters, the dominant effect is due to intergalactic medium (IGM) absorption. IGM treatment (Madau et al. 1996) and Galactic extinction corrections are included by IMPZ.
Internal extinction. Variable extinction is allowed in the fits via variable A_V added to the templates. A_V limits of 0–2 in the A_V freedom are used. As found in B04, the inclusion of A_V as a parameter gives an important improvement in the accuracy of the resulting redshifts, though from Babbedge, Whitaker & Morris (2005) it is also apparent that the derived extinction of the source is imprecise. With the inclusion of near-IR data in the fits, A_V freedom is now extended to the AGN fits, though restricted to $A_V \leqslant 0.3$ in order to prevent aliasing with normal galaxies (it was found that otherwise low-redshift galaxies could be fit as higher redshift AGN with high extinction).

A_V *Prior*. A prior expectation that the probability of a given value of A_V being 'correct' declines as $|A_V|$ moves away from 0 is applied. This is introduced by minimizing $\chi^2_{red} + \alpha A_V^2$ rather than χ^2 ($\alpha = 3$ here). This use of a prior can be viewed as a weak implementation of Bayesian methods and was reached based on degeneracy studies in B04 and Rowan-Robinson (2003), hereafter RR03.
Magnitude limits. RR03 and B04 found it necessary to apply absolute magnitude limits to exclude unlikely solutions (such as superluminous sources at high redshift). Here, the following limits are

used. Absolute magnitude limits of $-16 < M_B < (-22.5 + 0.3z)$ for galaxies and $-21.7 < M_B < -26.7$ for AGN.

A 'good' photometric redshift solution is chosen to be one with a $\chi^2_{red} < 10$. This value of χ^2_{red} is chosen as a threshold based on the results in B04 and in this paper since fits above this value are less reliable.

3.1.2 Comparison of spectroscopic and photometric redshifts

Investigations have been carried out for several data sets in the SWIRE fields, all of which have optical photometry, IR data from *Spitzer* and spectroscopic redshifts. RR05 previously demonstrated the success of the code for both an ELAIS-N1 sample and for a sample in the Lockman VF (the WIYN Survey; Owen et al., in preparation). It is worth noting that the results from the WIYN comparison showed the code is successful for galaxies out to $z > 1$, whilst earlier work on *Hubble Deep Field*-North (HDF-N) (RR03) and CDF-N (B04) samples have shown success for galaxies in the range $0 < z < 5$ and $0 < z < 2$, respectively, and for Type 1 AGN out to $z \sim 5$ (B04).

Here, updated results for several spectroscopic samples are outlined below, measuring the reliability and accuracy of the photometric redshifts via the fractional error $\overline{\Delta z}/(1 + z)$ for each source and examining the mean error $\overline{\Delta z}/(1 + z)$ and the rms scatter σ_z.

(i) *Lockman VF.* In the 0.3 deg^2 Lockman VF of the SWIRE Survey, there are U, g', r' and i' data, taken with the Mosaic I camera on the Mayall 4-m telescope at Kitt Peak National Observatory, and *Spitzer* 3.6–24 μm data. The comparison of photometric redshifts to 269 sources with spectroscopic redshifts from the WIYN Survey (Owen et al., in preparation) gives a rms scatter of 0.061, with galaxies out to $z \sim 1$, and Type 1 AGN out to $z \sim 3$. Compare this to typical accuracies of $\sigma_{red} \sim 0.1$ for studies considering only optical photometry in the fits (RR03).

(ii) *ELAIS-N1*. The spectroscopic redshift sample used in RR05 and Rowan-Robinson et al. (2004), comprising spectroscopic redshifts in ELAIS-N1 (reported by Pérez-Fournon et al., in preparation and Serjeant et al., in preparation; Hatziminaoglou et al. 2005b) with optical U, g', r', i', Z and J, H, K (where available) and *Spitzer* data. For this sample the total rms scatter, σ_{tot}, was 0.057, where the majority of sources out to redshift $z \sim 0.5$ are galaxies whilst at higher redshifts (to $z \sim 3$) Type 1 AGN dominate.

(iii) *VIRMOS-VLT Deep Survey*. Comprises optical photometry from the CFH12K-VIRMOS Survey (Le Fèvre et al. 2004): a deep BVRI imaging survey conducted with the CFH12K camera in four fields. Additionally, there are U-band data from the 2.2-m telescope in La Silla and J, K data from the New Technology Telescope (NTT). The spectroscopic redshifts come from the follow-up VIRMOS-VLT Deep Survey (VVDS) (Le Fèvre et al. 2003), a large spectroscopic follow-up survey which overlaps with the SWIRE data in the XMM-LSS field. For 1394 galaxies in the range $0 < z < 1.5$, the achieved accuracy was $\sigma_z = 0.052$ with very low systematic offset.

For all the samples, the mean systematic offset between the photometric and spectroscopic redshifts was found to be essentially zero to the precision of the photometric redshifts. For example, the ELAIS-N1 sample has $\overline{\Delta z}/(1 + z) = 0.0037$. In comparison to earlier results for the spectroscopic samples where photometric redshifts were derived from only the optical photometry (RR03; B04; Rowan-Robinson et al. 2004), the inclusion of the 3.6 and 4.5-μm data from *Spitzer* enables several solution degeneracies to be broken

Table 1. *Statistics from the catalogue.* Note that these statistics are for the full coverage region, prior to any IR flux cut imposed for LF calculations.

	3.6 μm	4.5 μm	5.8 μm	8 μm	24 μm
Enough bands for z_{phot}, N_{4band}	181 000	138 000	40 000	35 000	24 000
After stars removed, $N_{4band,exgal}$	140 000	105 000	26 000	25 800	23 500
Specify $17 < r' < 23$, $N_{4band,exgal,r}$	103 000	81 000	23 000	24 000	20 100
$N_{4band,exgal}$ with z_{phot} solution, N_z	134 000	99 500	25 600	25 500	22 800
$N_{4band,exgal,r}$ with z_{phot} solution, $N_{z,r}$	102 000	79 800	23 200	24 100	20 000
$N_{z,r}$ with $\chi^2_{red} < 10$, $N_{z,r\chi}$	96 200	74 700	20 500	21 600	18 200
$N_{z,r\chi}$, galaxies, N_{gal} and $\langle z \rangle$	88 600; 0.55	71 000; 0.55	19 700; 0.50	20 700; 0.40	17 300; 0.53
$N_{z,r\chi}$, ellipticals and $\langle z \rangle$	12 900; 0.38	12 500; 0.38	6 390; 0.36	4 470; 0.30	1 630; 0.28
$N_{z,r\chi}$, [Sab, Sbc, Scd, Sdm] and $\langle z \rangle$	52 600; 0.53	41 700; 0.54	11 100; 0.54	13 400; 0.41	11 500; 0.52
$N_{z,r\chi}$, starbursts and $\langle z \rangle$	23 100; 0.67	16 800; 0.71	2 260; 0.66	2 850; 0.51	4 130; 0.68
$N_{z,r\chi}$, optical AGN, N_{agn} and $\langle z \rangle$	7 610; 2.78	3 680; 2.57	756; 1.99	880; 2.01	914; 2.02
$N_{z,r\chi}$ with IR excess, N_{excess}	26 500	26 300	14 000	20 600	18 200
N_{excess} fit as cirrus	4 800	4 810	3 440	4 610	4 570
N_{excess} fit as M82	5 510	5 500	3 270	4 330	4 230
N_{excess} fit as Arp220	2 670	2 670	1 790	2 590	2 240
N_{excess} fit as AGN dust torus	5 160	5 150	3 400	3 470	4 290
N_{excess} single-band IR excess	8 303	8 190	2 050	5 600	2 840

since data are provided on the underlying SED across a much wider observed wavelength range (0.3–5 μm). The additional near-IR information has reduced the dispersion and has enabled the rejection of most of the extreme outliers resulting from optical-only results. This is an important improvement – even though the two IRAC bands may not have enabled a correct photometric redshift to be found for some of the original extreme outliers they have enabled the code to reject most of the original optical-only bad outliers, leaving fewer spurious redshift solutions.

From these studies, it is concluded that the inclusion of the first two IRAC bands in the photometric solution reduces the rms error and enables the rejection of the majority of catastrophic outliers. Furthermore, the inclusion of the first two IRAC bands in the solution reduces the rms scatter. Further information on photometric redshifts and their extension to IR wavelengths for the SWIRE Survey can be found in Babbedge (2004), RR05, Rowan-Robinson et al. (in preparation) and Andreon et al. (in preparation).

3.1.3 Application to the optical–Spitzer catalogue

The photometric redshifts of the optical–*Spitzer* extragalactic sources have been derived from their optical and IRAC 3.6-, 4.5-μm detections using the updated version of IMPZ with the setup set out in Section 3.1.1. The resulting photometric redshifts are expected to be accurate to ~0.05 in $\log_{10}(1 + z)$, based on comparison to the spectroscopic sample in Section 3.1.2 and the work of RR05, B04 and RR03.

Due to the aliasing and photometric variability issues noted in B04 (and also Afonso-Luis et al. 2004), the accuracy for the AGN will be lower, ~0.2 in $\log_{10}(1 + z)$. The study of SWIRE/*Chandra* sources by Franceschini et al. (2005) (F05) also found that the photometric redshift accuracy of their AGN was low, whilst Kitsionas et al. (2005) found that, for their X-ray selected *XMM–Newton*/2dF sample, the photometric redshift accuracy for AGN was <0.2 in $\Delta z/(1 + z)$ for 75 per cent of the sample, with indications of the need for a new set of templates in order to model the outliers. Here, in order to successfully deal with cases where there is significant dust torus contribution to emission at 3.6 and 4.5 μm, a 'double

pass' of the catalogue through IMPZ is carried out as described in Section 3.1.1.

Redshift results

Of the 139 823 extragalactic sources input to the code 96 per cent of sources obtain a photometric redshift solution. For the 102 645 sources with $17 < r' < 23$, there are only 800 redshift failures and there are 96 177 with solutions below the χ^2_{red} maximum of 10. It is this $17 < r' < 23$ sample with redshift solutions of $\chi^2_{red} < 10$ that we will make use of in the calculation of LFs (see Table 1 for statistics).

From the plot comparing of the r' magnitude distribution of sources that did and did not obtain a redshift (first panel of Fig. 2), one feature is apparent: the magnitude distribution of those sources that failed to obtain a redshift is bimodal–there is a small distribution of bright sources ($r' < 20$) which most likely failed to obtain a solution due to problems with saturated photometry and miss-associations of artefacts around bright stars and there is also a distribution of fainter sources ($r' > 21$) for whom failure can be attributed to the lower accuracy of photometry at fainter fluxes, the loss of bands towards the limiting depths and also to them being faint stars which were not picked out by the original star/galaxy separation.

We plot χ^2_{red} distributions of the photometric redshift solutions in Fig. 4, split into galaxy and Type 1 AGN template solutions. In each case, the distribution has been split into the same redshift bins as will be used for the various LF determinations in Section 4, and the typical proportion of galaxy and AGN solutions in each redshift bin with $\chi^2_{red} < 10$ is $\gtrsim$90 per cent. For the galaxy solutions, the slope of the χ^2_{red} distributions does not change with redshift, indicating that the applicability of the method and chosen templates remains successful out to the maximum redshift considered for the galaxy LF calculations. The slope of the χ^2_{red} distribution for the AGN solutions does show some variation, with indications that the solutions improve at the highest redshifts considered (3–4). This is attributed to the shifting into the optical bands of the Lyman break and IGM features in the AGN template which allows the AGN to be identified more readily.
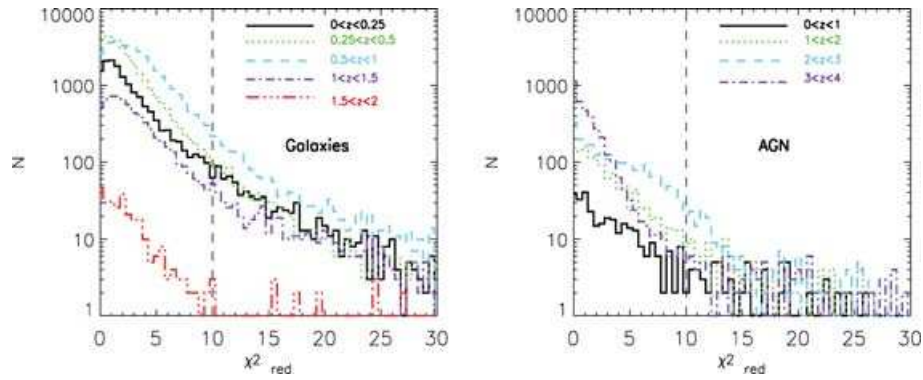
Figure 4. $\chi^2_{\rm red}$ of photometric redshifts for the different redshift bins considered. Left-hand panel is solutions for galaxies, redshift bins of [0–0.25] (black solid), [0.25–0.5] (green dotted), [0.5–1] (cyan dashed), [1–1.5] (purple dot–dashed) and [1.5–2] (red triple dot–dashed). Right-hand panel is solutions for AGN, redshift bins are [0–1] (black solid), [1–2] (green dotted), [2–3] (cyan dashed) and [3–4] (purple dot–dashed). Also shown is the maximum allowed $\chi^2_{\rm red} = 10$ cut-off.
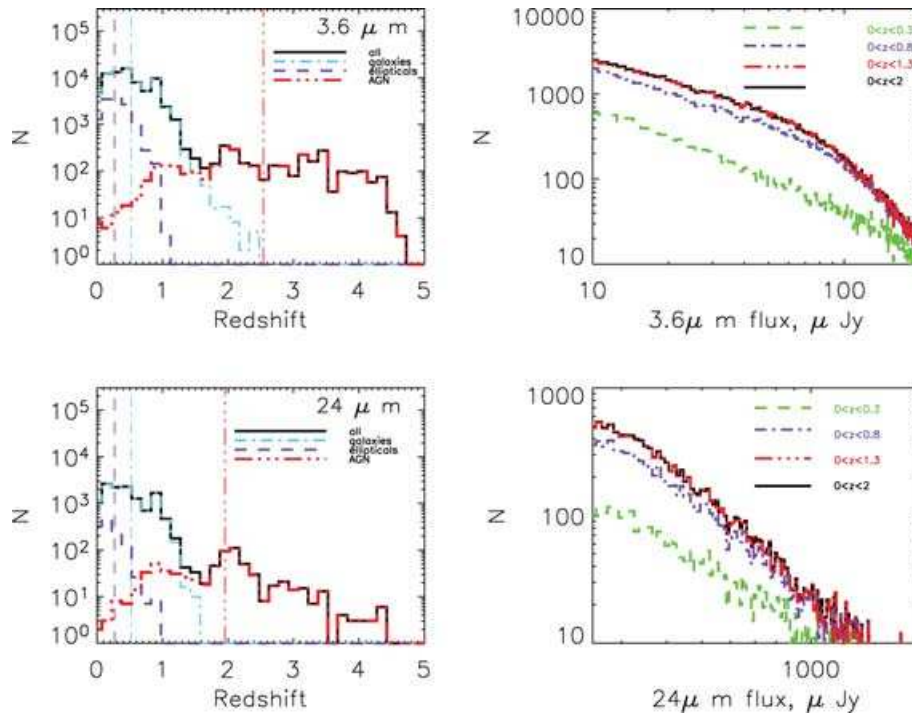
Figure 5. Photometric redshift distributions in selected *Spitzer* bands. Left-hand panels: $N(z)$ for all sources (black histogram); galaxy template solutions (E, Sab, Sbc, Scd, Sdm and starburst) are overplotted as light blue dot–dashed histogram; ellipticals are overplotted as purple dashed histogram; AGN solutions are overplotted as red dash–triple dot histogram. The mean redshift of each population is indicated by a vertical line; light-blue dot–dashed line (all galaxies), purple dashed (ellipticals), red triple dot–dashed (AGN). Right-hand panels: number counts for sources in several redshift ranges (not corrected for completeness).

Galaxy solutions

We plot redshift distributions of selected IR populations (3.6- and 24-μm sources[1]) on the left-hand panels of Fig. 5. The distributions for 4.5- and 5.8-μm sources are similar to the 3.6 μm whilst the 8-μm distribution starts to move towards the distribution seen for the 24-μm sources. The galaxy populations, with $\langle z_{\rm gal} \rangle = 0.55$, extend out to a redshift of around 1 before dropping away. For comparison, the

---

[1] At points in this paper, rather than present results in all bands, we focus only on the 3.6- and 24-μm results since they represent the two ends of the populations under study.

24-μm-selected (to 83 μJy) galaxy population of Pérez-González et al. (2005) (PG05) peaked at a redshift of 0.6–1, and decayed monotonically from redshift 1 to 3. A comparison of the galaxy redshift distributions to the models of Rowan-Robinson (2001), Xu et al. (2003) and Pozzi et al. (2004) is given in RR05 and indicates that the models manage to broadly reproduce the observed galaxy distribution, although the Xu et al. (2003) model predicts the peak to be at a higher redshift, of $z \sim 1$.

The distribution of sources indicate that below a redshift of $z \sim 0.5$, ~22 per cent of galaxies are early type (fit as ellipticals). Given that our template-fitting classification is by nature statistical rather than individual this compares favourably with detailed

morphological studies of *K*-selected galaxies with deep *Hubble* Advanced Camera for Surveys (ACS) imaging (Cassata et al. 2005; 20 per cent) and the 3.6-μm-selected galaxy population in the ACS field of UGC10214 (Hatziminaoglou et al. 2005a; 24 per cent). In the IRAC channels, the early-type population extends out to a redshift of around unity. Above this redshift, the number of sources drops away as the sensitivity of the survey to these sources is reached. The remainder of the galaxies are spirals and starbursts. These extend out to redshifts of around 1.5 before they start to drop below the sensitivities of the optical survey.

The proportion of early types in the 24-μm population drops to ∼15 per cent of the galaxy population. Traditionally, the IR emission from early types is expected to be low since they are old stellar populations with little dust or ongoing star formation, leading to some contribution to the IRAC bands but negligible contribution to 24 μm (e.g. *IRAS* observations of the Shapley–Ames sample found very little emission at 60 μm for ellipticals; de Jong et al. 1984; van den Bergh 2004). However, IR-luminous ellipticals are not unknown: for example, Leeuw et al.'s (2004) analysis of FIR-bright ellipticals suggested they contained cold dust in their central regions, whilst Krause et al.'s (2003) observations of one of the brightest 170-μm sources in the ISOPHOT Serendipity Survey showed it to be an elliptical with a postulated opaque hidden starburst in its centre.

The 24-μm population of early-type galaxies in SWIRE is therefore an interesting one–it may well turn out that the frequency of dusty early-type systems is greater than previously thought. As noted in RR05, it is likely that some of the elliptical template fits to 24-μm sources will be Arp220-like objects which, in the optical, have SEDs similar to elliptical-like systems due to the heavy obscuration of young stars. Similarly, late-type galaxies with significant dust extinction would appear, optically, to be reddened/early type. A recent spectroscopic study of SWIRE/SDSS (Sloan Digital Sky Survey) galaxies at low redshift (Davoodi et al. 2006) has shown a significant population of IR luminous galaxies have red optical colours that cannot be explained by optical extinction or contribution from AGN.

The mean redshift of the elliptical, spiral and starburst populations in each band can be found in Table 1.

In the right-hand panels of Fig. 5, we plot flux distributions of selected IR populations (3.6- and 24-μm sources) split into redshift ranges. These show a strong evolution from $z = 0$ to $z \sim 0.8$, but this evolution is not seen to continue to higher redshifts (as commented by PG05 and Chary et al. 2004b). These, however, are those *Spitzer* sources with an optical counterpart; the ∼30 per cent of sources which are optically blank might well be expected to lie at higher redshift – such as in the bimodal redshift distribution of Chary et al. (2004a) which predicts a second IR bright population centred around redshift ∼2.

Type 1 AGN solutions

8 per cent of SWIRE sources are identified by photometric redshift fitting as optical (Type I) AGN. F05's study of faint *Chandra* X-ray sources in ELAIS-N1 found the 24-μm population was 10–20 per cent AGN (Types 1 and 2) with a ratio of between 1:2 and 1:3 between Types 1 and 2. Hence, ∼5 per cent of the 24-μm sources were Type 1 AGN. As a comparison of the 18 200 24-μm sources with a good photometric redshift solution and $17 < r' < 23$, we find 914 optical Type 1 AGN fits, or 5 per cent. Although a detailed cross-analysis of X-ray-derived AGN fractions to the SED template fitting and compact morphology approach of this paper is

not conducted here, we have made a simple cross-match between the photometric redshift catalogue and the 99 X-ray sources from F05. Of the 50 matches, 16 are classed as optical Type 1 AGN from our photometric redshift SED fitting whilst F05 class 11 of these 16 as Type 1 AGN, four as Type 2, and one as a late-type galaxy. Thus our method is successful in identifying optical Type 1 AGN. There will, unavoidably, remain some Type 2 AGN 'contamination' in our galaxy samples–for example, of the four elliptical-SED sources that obtain a match to the F05 *Chandra* sample, the F05 designation was split into early type (2), galaxy (1) and Type 2 AGN (1) classes. More generally, F05 found that a significant fraction (up to 40 per cent) of IR sources classified as AGNs in the X-ray do not show any AGN evidence in the IR/optical SED – consider that all of our 18 200 24-μm sources have an IR excess, of which 23 per cent are fit in the mid-IR as AGN dust tori (i.e. Types 1 and 2 AGN). This implies a Type 1–2 ratio of 1:4 or 5 since only 5 per cent are fit as a Type 1 AGN in the optical. This is the canonical fraction one finds from standard X-ray background (XRB) models, but these tend to be driven by Type 1 AGN work, which peak at $z \sim 2$ say, whereas F05 found the ratio was reduced due to XRB contribution from Type 2 sources at moderate to low redshift. Given this we would expect the obscured Type 2 to be 'hidden' in the galaxy LF's – the reader is cautioned to keep this caveat in mind when interpreting the results, particularly at the longer *Spitzer* wavelengths where it is notoriously difficult to disentangle AGN/starburst contributions.

The AGN are seen to be a population that extends across the full redshift range, with a slight peak in their distribution at a redshift of around two, and a tail to high redshift. This slight rise to redshift two, and decline thereafter, is as predicted by the new version of Xu et al.'s (2003) models when including a new evolutionary model for dusty galaxies and the SWIRE limits. This predicted AGN distribution was given in Hatziminaoglou et al. (2005b).

Above a redshift of around two, the AGN solutions dominate over the galaxy counts, though this is mainly due to SWIRE's ability to detect them to higher redshift.

3.2 Mid-IR SED fitting

Mid-IR template fitting is carried out in a technique described in RR05. A source that has been fit with an optical to near-IR galaxy template, based on its *U* band to 4.5-μm detections as set out in Section 3.1, now has its IR excess calculated by subtracting the galaxy model fit prediction from the 4.5- to 24-μm data.

At least two of these bands then need to exhibit an IR excess (one of which is required to be 8 or 24 μm). This excess is then characterized by finding the best-fitting out of a cirrus (Efstathiou & Rowan-Robinson 2003), M82 and Arp220 starbursts (Efstathiou, Rowan-Robinson & Siebenmorgen 2000) or AGN dust torus IR template (Rowan-Robinson 1995) (shown in Fig. 6). More information on these templates can be found in RR05. Here, it is merely noted that each template is the result of radiative transfer models and that although for *individual* galaxies one could obtain better *individual* fits using radiative transfer codes, we here wish to characterize only the broad types of IR population. This 'first-order' approach is in fact remarkably effective and a blind comparison of predicted 70-μm flux (without making use of the 70-μm information) derived from the mid-IR SED fitting method adopted here to the observed 70-μm fluxes produces impressive agreement for all four mid-IR templates, across almost two orders of magnitude in 70-μm flux (see fig. 5 of Rowan-Robinson et al. 2006).

Sources are also allowed to be fit by a mixture of an M82 starburst and cirrus since it was found that, often, both components
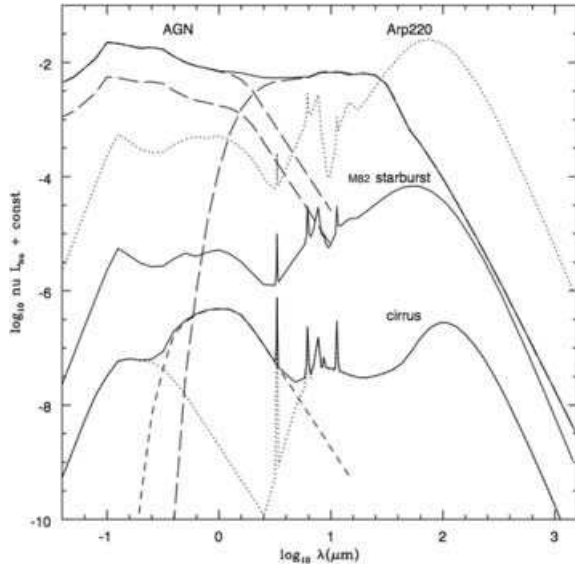
Figure 6. Mid-IR spectral energy distributions: four components – cirrus [split into low-mass (dashed line) and high-mass (dotted line) components in the optical region], M82-like starburst (solid line), Arp220-like starburst (dotted line) and AGN torus, showing assumed optical/IR ratio at $\log L_{60} = 14$ (upper curve) and 8. Taken from Rowan-Robinson (2001).

were required to properly represent the IR excess. This mirrors the conclusions of Rowan-Robinson & Crawford (1989) from fitting mid-IR SEDs to *IRAS* sources, and the findings of RR05.

For an IR SED to be fit, then, there needs to be an IR excess. If this is not the case then a mid-IR template-based K-correction, K_{IR}, is not calculated for the source and the extrapolated mid-IR contribution from the optical/near-IR template fit is used instead for in the calculation of $z_{max,IR}$ (see Section 4). In the case of a single band IR excess, a M82 SED is assumed. Statistics for the IR excess sources are given in Table 1.

4 LF PROCEDURE

Now that the optical/near-IR and mid-IR SEDs of each source have been characterized and their photometric redshifts determined, this information can be used to calculate LFs, and to include K-corrections derived from the model templates.

Provided a selection function can be defined, a general LF is calculable so long as there is no significant population of objects which remain undetected at *any* redshift.[2] Assuming that we have a sufficiently detailed selection function (see Section 4.1) and that no such *invisible* population exists–a reasonable assumption given that local galaxies can all be expected to be detected in some of the multivariate wavelengths under consideration – we can use the $1/V_{max}$ method (Schmidt 1968 and extended by Avni & Bahcall 1980) to determine LFs for each *Spitzer* waveband.

In this, the LF, $\Phi(L)$, is calculated using the $1/V_{max}$ method, where V_{max} is the volume corresponding to the maximum redshift at which a source could be detected by the survey. This maximum redshift may be set by either the optical limits ($r' < 23$), or the IR limits, as determined by using K-corrections calculated from the

[2] There is also a possibility that so few galaxies of a population are detected that a selection function cannot be derived for them. Some discussion of potential bias is given in Section 4.2.

optical/near-IR and mid-IR template fits. We choose to be conservative in our choice of IR flux limits (to minimize incompleteness and maintain reliability, see Section 4.1), setting the lower IR flux limit below which a source is not considered for a given LF calculation to be 30 µJy (3.6 µm), 30 µJy (4.5 µm), 50 µJy (5.8 µm), 50 µJy (8 µm) and 500 µJy (24 µm).

Thus,

$$\Phi(L)\,dL = \sum_i \frac{1}{V_{max,i}}, \tag{1}$$

where $\Phi(L)$ is the number of objects per Mpc^3 in the (rest frame) luminosity range L–$(L+dL)$ and

$$V_{max,i} = \min(V_{optical,i}, V_{IR,i}). \tag{2}$$

Therefore, for the case of the rest frame 3.6-µm LF, $V_{IR,i}$ is obtained by taking the source in question and redshifting it until its observed flux at 3.6 µm drops below the chosen limit of 30 µJy. $V_{optical,i}$ corresponds to the maximum redshift out to which the same source would be detectable, down to the chosen magnitude limit of $r' = 23$ (in order to minimize incompleteness and photometric inaccuracy, see Fig. 2).

The associated rms error, from Poisson statistics, is given by

$$\Delta\Phi(L) = \sqrt{\sum_i \frac{1}{V_{max,i}^2}}. \tag{3}$$

To find $V_{optical,i}$, we find the redshift, $z_{max,optical}$, at which the optical apparent magnitude, $m(z)$, of a source of absolute magnitude, M, when redshifted to a redshift, z, becomes fainter then the chosen limiting magnitude of the survey ($r' < 23$), where $m(z)$ is given by

$$m(z) = M + 5\log_{10}\left(\frac{D_L}{10\,pc}\right) + 2.5\log_{10}K_{opt}. \tag{4}$$

Here, D_L is the luminosity distance to redshift z, and K_{opt} is the K-correction. K_{opt} also includes the increased effect of IGM absorption at higher redshifts (Madau et al. 1996). K_{opt} is defined as

$$K_{opt}(z) = (1+z)\frac{\int F(\lambda)S(\lambda)\,d\lambda}{\int F\left(\frac{\lambda}{1+z}\right)S(\lambda)IGM(\lambda,z)\,d\lambda}, \tag{5}$$

where $F(\lambda)$ is the optical SED template at source, $S(\lambda)$ is the combined filter transmission and CCD response curve and $IGM(\lambda, z)$ is the redshift-dependent IGM transmission.

Similarly, for $V_{IR,i}$, we find the redshift, $z_{max,IR}$ at which the IR flux in the IR band in question, $S_{IR}(z)$, of a source of absolute monochromatic luminosity, L_{IR}, when redshifted to an arbitrary redshift, z, becomes fainter than the chosen limiting flux of the survey. The K-correction, K_{IR}, is defined as in equation (5), with $F(\lambda)$ now the IR SED template at source and $S(\lambda)$ is the chosen IR filter transmission. For IR K-corrections, we do not need to incorporate IGM transmission effects for the redshifts considered.

In order to calculate the LFs correctly, however, we need to use a weighting function on the volumes in order to correct for the various selection biases that are inherent in the catalogue. This is set out in Section 4.1.

When calculating the LFs, galaxies with redshifts above two are cut since the reliability of their photometric redshifts is lower (and the availability of spectroscopic redshifts to validate the redshift code is low) and they can have a large effect on the bright end of the LF, particularly given the low number of sources above this redshift. This excludes ∼0.2 per cent of the sample. Similarly, AGN with redshifts above four are cut. Due to photometric variability, the reduced accuracy of photometric redshift techniques when applied

to AGN and the sparser opportunities for spectroscopic redshift validation this cut is prudent, excluding ∼5 per cent of the sources fit in the optical by AGN templates.

We choose to split the LFs into different redshift bins in order to probe evolution. For redshift bins, the LF calculation is slightly modified, in that the minimum redshift of the redshift bin in question needs to be subtracted from the $V_{\mathrm{max},i}$ in equation (2). The sources are split into galaxies and AGN based on their best-fitting optical/near-IR template and for these two samples LFs are constructed in the following redshift bins.

(i) For galaxies, LFs are constructed in the redshift bins [0–0.25], [0.25–0.5], [0.5–1], [1–1.5] and [1.5–2].

(ii) For AGN (smaller number statistics and broader redshift range), LFs are constructed in the redshift bins [0–1], [1–2], [2–3] and [3–4].

4.1 Incompleteness and selection functions

The data set used to calculate the LF in each IR band is a biased sample. This is due to the multivariate flux limits imposed in order for a source to be included in the calculations and the requirements that it has enough information to be passed to the redshift and IR SED fitting codes *and* obtain a solution (with $\chi^2_{\mathrm{red}} < 10$). The general procedure for deriving an overall selection function is the same regardless of the IR band in question. Here, the 24-μm LF will be used as an example.

The starting point for the 24-μm LF calculation is the SWIRE *extragalactic* catalogue (so stars have been removed and $17 < r' < 23$) further cut to $S(24) > 500\,\mu$Jy (the chosen 24-μm flux limit from Section 4). The probability that a source of a given flux at 24 μm is detected by the survey, $\eta_{\mathrm{detec}}(S)$ has been determined by Shupe et al. (in preparation) – for IRAC see Surace et al. (2005). Then, in order to be passed to the photometric redshift code, it needs to have detections in at least four of the bands used to calculate redshift (optical, 3.6 and 4.5 μm, two of which need to be 3.6 μm and r'. This is characterized by $\eta_{\mathrm{pz,in}}(S_{24})$. The source then needs to obtain a solution with $\chi^2_{\mathrm{red}<10}$, as characterized by $\eta_{\mathrm{pz,out}}(S_{24})$.

Thus, the probability that a given 24-μm source has sufficient information to be passed to the photometric redshift code, $\eta_{\mathrm{pz,in}}(S_{24})$, is calculated in the following manner.

We take the input catalogue and construct a source count distribution, $N_{\mathrm{all}}(S)$. We then find all those sources which are eligible for photometric redshift calculation and construct a similar source count distribution, $N_{\mathrm{pz,in}}(S)$. Dividing one by the other gives the selection bias, as a function of 24-μm flux:

$$\eta_{\mathrm{pz,in}}(S) = \frac{N_{\mathrm{pz,in}}(S)}{N_{\mathrm{all}}(S)}. \tag{6}$$

Similarly, we can calculate the selection bias, $\eta_{\mathrm{pz,out}}(S_{24})$, introduced by requiring a source to receive a redshift solution with $\chi^2_{\mathrm{red}} < 10$, by constructing the source count distribution, $N_{\mathrm{pz,out}}(S)$, of all sources which did obtain a good redshift solution, and obtain the resulting selection bias via

$$\eta_{\mathrm{pz,out}}(S) = \frac{N_{\mathrm{pz,out}}(S)}{N_{\mathrm{pz,in}}(S)}. \tag{7}$$

An overall selection bias, $\eta(S_{24})$, as a function of 24-μm flux is then the combination of these functions, namely,

$$\eta(S) = \eta_{\mathrm{detec}}(S)\eta_{\mathrm{pz,in}}(S)\eta_{\mathrm{pz,out}}(S). \tag{8}$$

The resulting selection functions for each IR band are given for IRAC and MIPS 24 μm in Fig. 7. Following Serjeant et al. (2001),
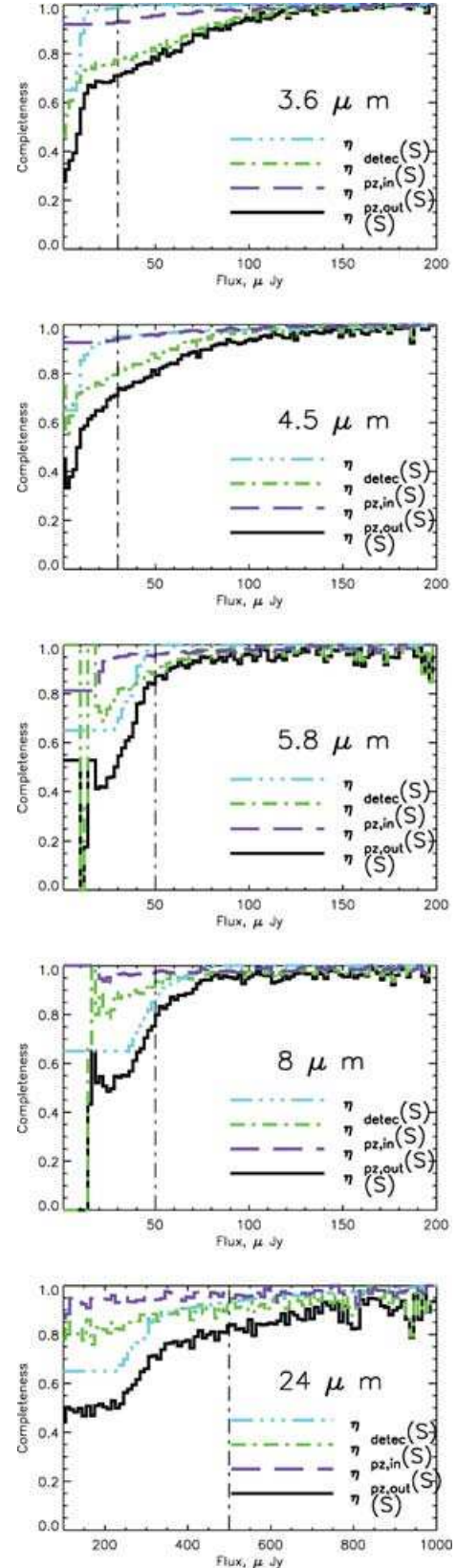

Figure 7. IRAC and 24-μm selection functions. The chosen flux limit for each band is shown as a vertical dot–dashed line.

these selection functions are used to weight the contribution of each source to the volume element integral in the LF calculation by modifying the volume elements in equation (1) to become

$$V'_{\mathrm{max},i} = \int_0^{z_{\mathrm{max},i}} \eta(z, S_i) \frac{\mathrm{d}V}{\mathrm{d}z} \, \mathrm{d}z. \tag{9}$$

It is important to note that this process will not be able to fully account for blank-field sources–those sources detected by *Spitzer* but absent from the optical catalogues and so having an undetermined redshift distribution. This is one reason for the choice of conservative IR flux limits. After implementation of the lower flux cut, requiring $17 < r' < 23$ and specifying a photometric redshift solution with $\chi^2_{\mathrm{red}} < 10$, the number of sources contributing to the LF calculation is as follows.

For 3.6-μm LF calculation – 34 281 sources.
For 4.5-μm LF calculation – 34 281 sources.
For 5.8-μm LF calculation – 13 623 sources.
For 8-μm LF calculation – 17 386 sources.
For 24-μm LF calculation – 4800 sources.

4.2 Bias

LFs are the result of complex selection functions and corrections for incompleteness required to account for the biases and limits introduced by observational selection effects.

The LFs calculated here are the sum of the LFs of each galaxy type. As such, there will be bias if certain galaxy types are not visible in a given redshift bin. However, even when they are, there will still be a potential bias if they are observable in different absolute magnitude ranges (Lilly et al. 1996; Brown et al. 2001). There are several different LF estimators, each with their own advantages and drawbacks (e.g. Willmer 1997; Takeuchi, Yoshikawa & Ishii 2000). The different biases each method can introduce to the LF were explored by Ilbert et al. (2004) who considered the dependence of limiting absolute magnitudes and the intrinsic bias introduced by the differing LFs of different galaxy populations. The classical $1/V_{\mathrm{max}}$ estimator (Schmidt 1968), as used in this paper, accounts for the apparent magnitude limit of a survey by assuming a homogeneous galaxy distribution. It has been shown that this assumption is not robust to clusters or voids (Takeuchi et al. 2000), but this should be less of an issue for the 6.5 square degree field and large redshift range used here. An advantage is the simplicity of the method and that it is able to give the shape and normalization of the LF at the same time. Ilbert et al. (2004) found that the $1/V_{\mathrm{max}}$ method acts to underestimate the LF at the faintest luminosity bins, biasing the global LF faint-end slope. This was because beyond the absolute magnitude, where a certain galaxy population is not observable, the method recovers the LF slope of the remaining populations. For the $1/V_{\mathrm{max}}$ LF calculated here, there is therefore a potential that the faint end of the LFs has been underestimated. In general, however, if the selection function as a function of flux and redshift is accurate, the $1/V_{\mathrm{max}}$ will give an unbiased estimate.

The second consideration for the LFs calculated here is that they are based on photometric redshifts. One approach is to assume the photometric redshift is true for each source (as in other studies, such as Gwyn & Hartwick 1996; Mobasher et al. 1996; Sawicki, Lin & Yee 1997; Takeuchi et al. 2000). This leads to potential problems with the derived LF, which have been minimized to some extent by excluding poor χ^2_{red} solutions, only calculating the LFs in the redshift range where the photometric method has been tested to a reasonable extent (z of 0–2 for galaxies and z of 0–4 for AGN), and by using generous redshift bin widths. Despite this, the effect on the LF is a

systematic one, tending to increase the number density at the bright end of the LF since the combination of redshift uncertainty and the steep slope of the LF at the bright end serves to scatter more sources to higher rather than lower luminosity. As a result, the LF becomes flatter than the intrinsic LF at the bright end (see Chen et al. 2003 for an in-depth discussion). In order to obtain a more quantitative measure of the effect on the LF of the photometric redshifts, we here carry out Monte Carlo simulations where each photometric redshift is assumed to be sampled from an underlying Gaussian distribution. This will enable the effect of photometric redshift uncertainty to be quantified in the LF bins.

Monte Carlo analysis

Each source's photometric redshift is assumed to be sampled from an underlying Gaussian distribution with a width, σ, that is dependent on both the redshift and template type of the photometric redshift solution. This dependence is chosen since the accuracy of the photometric redshift method varies with redshift and is poorer for AGN in comparison to galaxies (from the studies in Section 3.1 and B04). Consider the following.

(i) *Galaxies.* At lower redshift, $z \lesssim 0.5$, the source will typically have good photometry and SED features, such as the Balmer break, are well bracketed by the filters. At higher redshift, $0.5 < z < 1.4$, there is still a reasonable bracketing of the main SED features by the filters, but the photometry is poorer. Hence, the accuracy of the photometric redshift is reduced, though it has been shown by numerous groups that for galaxy samples so far tested the accuracy of photometric redshift methods is within $\sigma_z < 0.1$ (Connolly et al. 1997; Fernández-Soto et al. 2001; RR03; B04; RR05). At still higher redshifts, $z > 1.4$, the Balmer break has left the z' filter, but the Lyman limit feature will not reach the U band until a redshift of 2.5. Coupled with increasingly faint sources, the redshift accuracy can be expected to be further reduced.

(ii) *AGN.* Again, at low redshift, $z < 0.5$, the source will be brighter and the photometry well determined (aside from photometric variability). At higher redshift, $0.5 < z < 2.5$, the photometric accuracy is reduced, mainly due to degeneracies between different emission lines. At high redshift, $z > 2.5$, the source has become fainter, but the Lyman limit SED feature has now entered the filters, improving the redshift identification (i.e. the Lyman dropout technique).

Based on these considerations, the relevant Gaussian is defined for each source in Table 2.

In order to carry out the Monte Carlo analysis, each source's photometric redshift is replaced by a redshift drawn randomly from the Gaussian distribution centred on the original photometric redshift (with the specification that the new redshift cannot be less than zero).

Table 2. *Gaussian parameters.* The chosen σ of the underlying Gaussian distribution adopted for the Monte Carlo alteration of the photometric redshifts. This σ refers to a Gaussian centred on the photometric redshift, in $\log(1+z)$ space.

Galaxies		AGN	
Redshift interval	σ	Redshift interval	σ
$0 < z_{\mathrm{phot}} < 0.5$	0.05	$0 < z_{\mathrm{phot}} < 0.5$	0.1
$0.5 < z_{\mathrm{phot}} < 1.4$	0.1	$0.5 < z_{\mathrm{phot}} < 2.5$	0.2
$z_{\mathrm{phot}} > 1.4$	0.15	$z_{\mathrm{phot}} > 2.5$	0.15

The usual LF procedure is then carried out. This is carried out 100 times, for the LF in each *Spitzer* band, thus producing a series of LFs for a given band. The rms spread in these LFs then represents the uncertainty introduced by using photometric redshifts instead of the true redshifts and this Monte Carlo-derived error is found to dominate over the Poisson-derived LF error, except in the least-populated luminosity bins (the highest redshifts and luminosities). The error in the AGN LFs will be larger since the photometric redshift technique is less accurate for AGN, due to their photometric variability over the time-scale of the optical survey.

5 RESULTS

5.1 Galaxy LFs with redshift

The galaxy LFs are plotted in panels of Fig. 8, with errors derived from the Monte Carlo treatment.
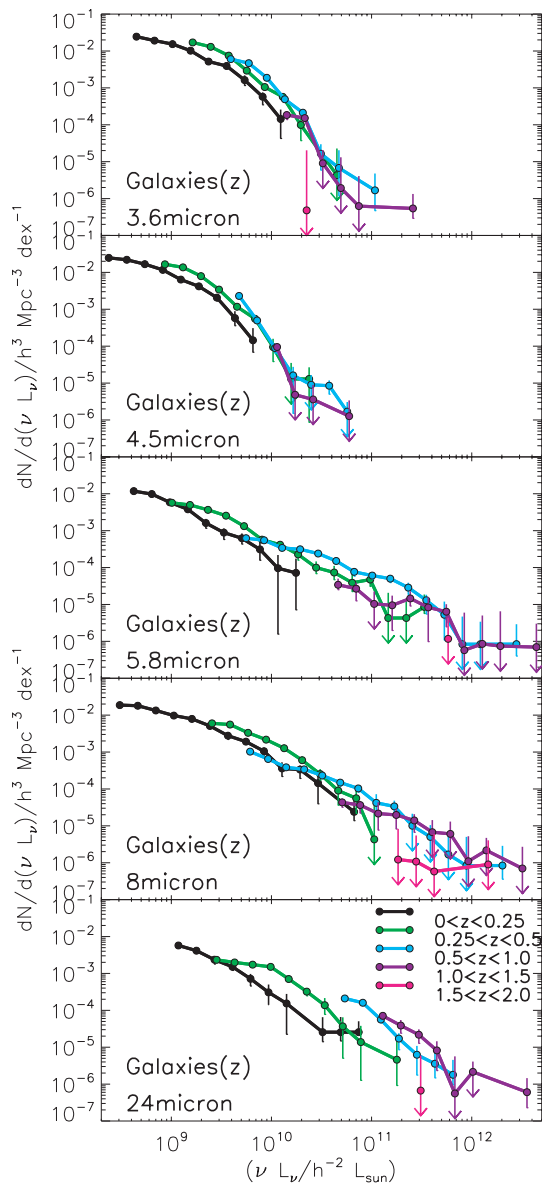
Figure 8. Galaxy LFs. Top panel to bottom panel: LF for galaxies at each wavelength (excluding AGN), split into redshift bins of [0–0.25] (black), [0.25–0.5] (green), [0.5–1] (cyan), [1–1.5] (purple) and [1.5–2] (pink).

The galaxy LF at 3.6 and 4.5 μm exhibits the classical Schechter functional form (Schechter 1976) which reflects the galaxy mass function (e.g. Fontana et al. 2004; Bundy, Ellis & Conselice 2005). That is, the 3.6- and 4.5-μm LFs are sampling the stellar mass of the galaxies since the bulk of emission at these wavelengths still arises from the older stellar populations. At the longer *Spitzer* wavelengths, the LF is then essentially sampling the SFR via dust emission, and the characteristic break seen at shorter wavelengths is less prominent. The bright upturn (for $L > 3E10 \, \nu L_\nu / h^{-2} \, L_\odot$) seen in the low redshift, $z < 0.25$, 24-μm galaxy LF in Fig. 8 can be plausibly attributed to the contribution of obscured AGN since, as discussed in Section 3.1.3, we expect an increasing input from Type 2 AGN to our galaxy LFs at the longer *Spitzer* wavelengths due to the classification criteria we use (optical Type 1 AGN or galaxy).

At the shorter wavelengths, these LFs do not demonstrate strong evolution where the results are consistent with a passive pure luminosity evolution (PLE) to higher luminosity/redshift. The most obvious evolution is seen at the longest wavelength (24 μm), where for the first three redshift bins this evolution can be seen as a general strong increase in luminosity with redshift. The two highest galaxy redshift bins ($z > 1$) do not show a strong continuation of this trend. Across all five bands, we find that the numbers of galaxies in the highest redshift bin ($1.5 < z < 2$) are not sufficient to properly characterize the galaxy LF at this epoch, but the results hint at a drop in space density.

One might additionally expect that different types of galaxy exhibit a different LF due to their differing formation and evolution history. We can use our broad-brush SED characterizations in order to examine the galaxy LFs with source type. The photometric redshift template-fitting approach allows us to constrain the redshift, and to loosely constrain the source type – that is, the characterizations are valid in a large-scale statistical sense but have less meaning for individual sources. The ability of photometric redshift codes to reliably recover galaxy type in addition to redshift is not well quantified since the method often relies on clear SED features such as the Balmer break which are found across several galaxy types. The study of Bolzonella, Miralles & Pelló (2000) found, however, that the success rate for bursts and ellipticals was high since they differ markedly from more intermediate types. Thus, here we choose to split the galaxy LFs by optical SED template type, into three subclasses (named so as to avoid morphological inferences): early type, 'late type' (Sab, Sbc, Scd and Sdm) and starbursts, with this caveat in mind.

The LFs of these subclasses are plotted in subpanels of Fig. 9 for the 3.6- and 24-μm populations. In each panel, the LFs for each subclass are shown broken down into each redshift bin. From this procedure, we see that the 3.6-μm late-type and starburst galaxy populations increase in activity out to $z \sim 1$. The early types do not contribute significantly to the evolution, and are consistent with a population formed at high redshift and then dimming as they age. The evolution in the 24-μm galaxies is also seen to be due to late types and starbursts in the range $z \sim 0.25–1$, and at both wavelengths the results would support an increase in the frequency of starbursts (and hence by implication, mergers) in the past.

The study of Franceschini et al. (2006) combined multiwavelength data in the *Chandra* Deep Field South, including very deep optical and near-IR photometry, deep [$S(3.6\,\mu m) > 1\,\mu Jy$] IRAC data and complementary optical spectroscopy. Importantly, they were able to differentiate reliably between early- and late-type classes out to high redshift and thus confirmed evidence for 'downsizing' occurring in galaxy formation such that more massive galaxies completed their star formation and star accumulation earlier than
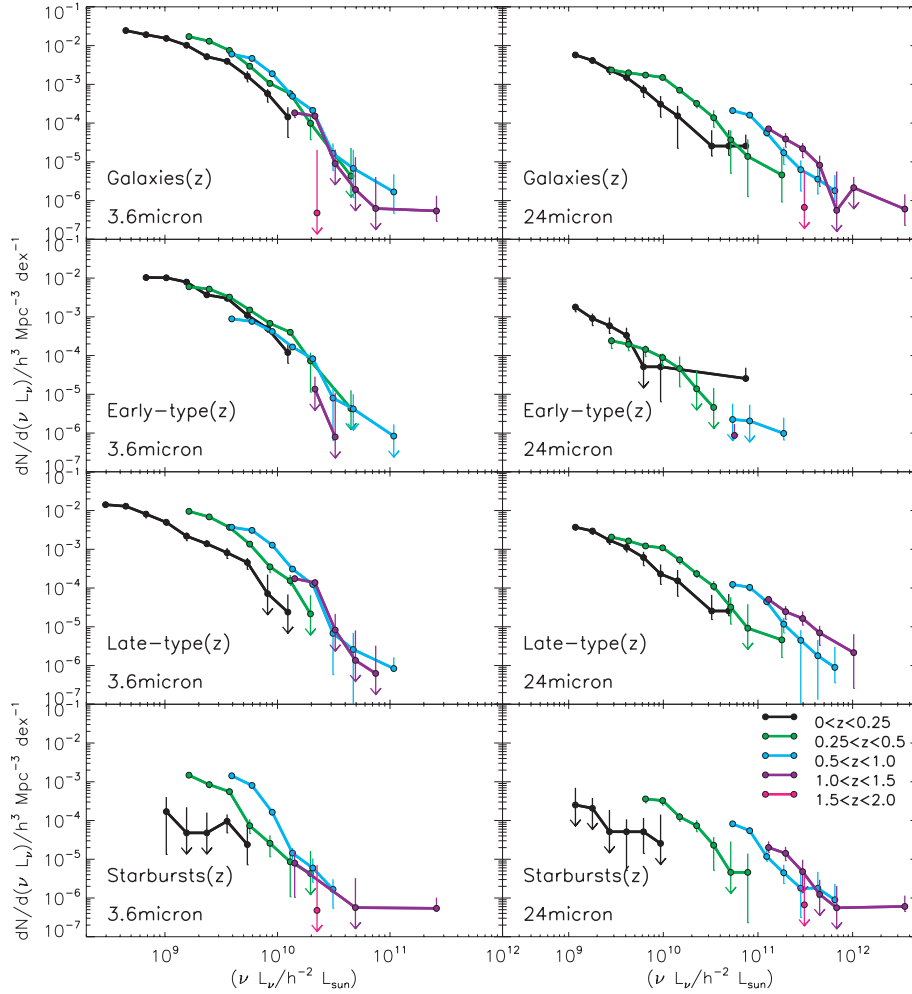
Figure 9. Selected galaxy LFs–3.6 and 24 μm. First row: LF for galaxies (excluding AGN), split into redshift bins of [0–0.25] (black), [0.25–0.5] (green), [0.5–1] (cyan), [1–1.5] (purple) and [1.5–2] (pink). Second row: LF for ellipticals, split into the same redshift bins. Third row: LF for spirals, split into the same redshift bins. Fourth row: LF for starbursts, split into the same redshift bins.

less massive ones. Their interpretation was that of a morphological shift from the star forming to the passively evolving phase (due to mergers and gas reduction) from high to low redshift, something only hinted at by the population breakdown shown in Fig. 9. It is of interest to note that the 3.6-μm LF for starbursts (bottom left-hand panel of Fig. 9) shows little evolution at high luminosity and more marked evolution at lower luminosity, as would be expected if less massive/luminous galaxies remained active to later epochs.

The depth of the survey does not allow strong conclusions to be made about the behaviour of early types above $z \sim 1$. The elliptical template used is of order 10 Gyr in age, though stellar synthesis models indicate that this should be reasonably similar to galaxies as young as 4 Gyr after an instantaneous burst (e.g. Bruzual & Charlot 1993, 2003). Galaxies younger than this will appear bluer and more like intermediate-type galaxies. Since the age of the Universe ranges from ~3.1 to ~5.6 Gyr in the range $2 < z < 1$, we would expect few galaxies to be fit well by our elliptical template at these redshifts.

5.2 Type 1 AGN LFs with redshift

The Type 1 AGN LFs are plotted as a function of redshift in each *Spitzer* band in the Fig. 10. Since the Type 1 AGN are a smaller population and suffer less precise redshifts, the resulting LFs are

noisier. However, the results are clear enough to show positive evolution out to at least the third redshift bin ($2 < z < 3$), with the strongest evolution in the range $1 < z < 2$.

One feature is seen at 24 μm, where the LF in the $1 < z < 2$ and $2 < z < 3$ is very similar (as compared to 8 μm, where evolution is seen when moving from $1 < z < 2$ to $2 < z < 3$). The statistical significance of this would need large-scale spectroscopic analysis for a proper interpretation but is likely to be, at least in part, due to the SED shape in these ranges–although both 8 and 24 μm are being dominated by hot dust emission from an AGN for these redshifts, the 8-μm emission corresponds to the rising part of the torus just after the minimum at 1 μm, whilst 24 μm traces the peak of the torus emission, plus silicate emission. Thus, variations in the exact SED could lead to differences in the observed LF in these bands with redshift, with, for example, the presence of the silicate feature in the 24-μm band at $z \sim 1.3$ boosting the $1 < z < 2$ LF luminosities.

6 OTHER STUDIES

6.1 Galaxies

The IRAC 3.6- and 4.5-μm galaxy LFs can be compared to near-IR LFs in the J (1.25 μm) and K_s (2.2 μm) bands which, similarly,
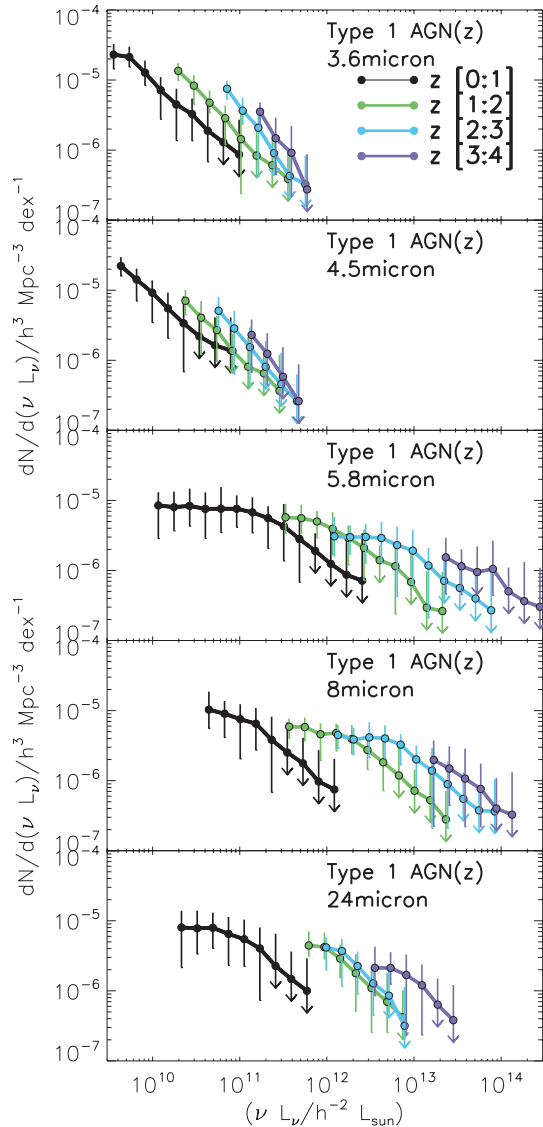
Figure 10. Type 1 AGN LFs. LFs for sources fit by IMPZ as Type 1 AGN, split into redshift bins of [0–1] (black), [1–2] (green), [2–3] (cyan) and [3–4] (purple).

Figure 11. Comparison of 3.6-μm galaxy LF to similar work. Solid circles joined by solid lines is the 3.6-μm galaxy LF of this work, split into redshift bins of [0–0.25] (black), [0.25–0.5] (green), [0.5–1] (cyan), [1–1.5] (purple) and [1.5–2] (pink). The results of Franceschini et al. (2006) are shown as stars, for the redshift intervals [0.1–0.55] (red), [0.55–0.9] (green) and [0.9–1.4] (white).

probe the stellar mass in galaxies. The J and K_s LFs of Pozzetti et al. (2003) found no evidence of steepening of the faint end of the LFs up to a redshift of ~1.3 and no evolution of the faint end, whilst finding positive luminosity evolution at the bright end of the LFs. Their mild evolution to $z \sim 1.5$ is in agreement with previous indications (Cowie et al. 1996; Cole et al. 2001; Cohen 2002; Feulner et al. 2003). The more recent 3.6-μm LF of Franceschini et al. (2006), for which half the sources had spectroscopic redshifts, extends out to $z \sim 1.4$ and demonstrates a trend for increasing luminosity consistent with the dominant stellar populations becoming younger at higher redshift.

Fig. 11 compares the 3.6-μm Franceschini et al. result to this work's 3.6-μm galaxy LF. The agreement between the two works is excellent, and can be considered a validation of the photometric redshift and mid-IR fitting approach used here. Though not over-plotted for reasons of clarity the Pozzetti et al. results, shifted from K_s band to 3.6 μm, are also in close agreement.

The 24-μm galaxy LF is compared to the local LF at 25 μm constructed by Shupe et al. (1998) from *IRAS* data to the *ISO*
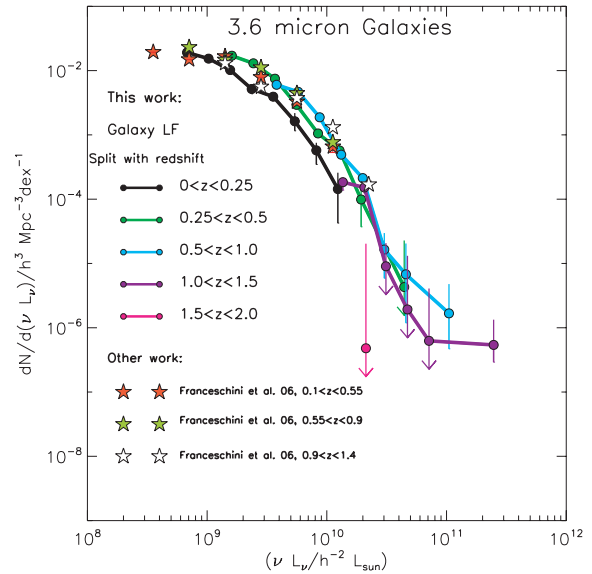
15-μm LF of Pozzi et al. (2004), to the deep 24-μm LF of PG05 and to the spectroscopic 24-μm LF of Onyett et al. (2005) from the SWIRE Lockman VF. This comparison is split into three broad redshift ranges and LFs have, where necessary, been converted to 24 μm using an assumed continuum shape of −0.5 for comparison purposes.

In Fig. 12, the 'low redshift', $z < 0.25$, 24-μm galaxy LF is considered. Shupe et el.'s local 25-μm LF follows the low-redshift sample of our 24-μm LF well, as does the 15-μm LF of Pozzi et al. (median redshift of 0.18) and the low-redshift sample from Onyet et al. ($z < 0.36$). The comparison to PG05 ($z < 0.2$) demonstrates the complementary nature of the data sets used – the deeper PG05 data are able to probe the LFs to fainter luminosities whilst the wider SWIRE data allow one to go to higher luminosities. In the region of overlap, the two results agree well. The bright upturn seen in our $z < 0.25$, 24-μm galaxy LF for $L > 3E10 \, \nu L_\nu / h^{-2} \, L_\odot$ can be plausibly attributed to the influence of obscured Type 2 AGN which remain in our 'galaxy' selection and start to have an influence at the highest luminosity (particularly at these low redshifts, where Type 2 AGN are more numerous).

In Fig. 13, the 'intermediate redshift', $0.25 < z < 1$, 24-μm galaxy LFs are compared to the higher redshift sample of Onyett et al. ($z > 0.36$), which exhibits a similar strong evolution at the bright end to the intermediate-redshift bins of this work. The median redshift of the Onyett et al. sample is 0.29, with 38 per cent of the sample in the $z > 0.36$ bin and the most distant source at $z \sim 2.9$. The intermediate redshift LFs from PG05 are also plotted.

PG05's highest redshift results, $0.8 < z < 1.8$, are compared to ours, $1.0 < z < 2.0$, in Fig. 14. Despite the slightly disparate redshift bin ranges and luminosities sampled, the two results are surprisingly good for these distant populations.

In summary, then, the SWIRE LFs derived using a large photometric data set have shown good agreement with other comparative
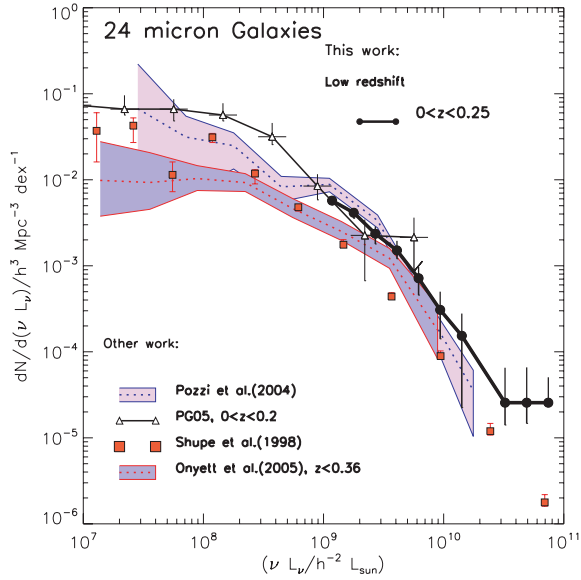
Figure 12. Comparison of 24-μm galaxy LF to similar work: low redshift. The solid coloured lines joining the circles are the LF of this work. This is then compared to the 25-μm LF of Shupe et al. (1998) to the 15-μm LFs of Pozzi et al. (2004), to the spectroscopic 24-μm LF of Onyett et al. (2005) from the SWIRE Lockman VF and to the 24-μm LF of PG05. The Onyett et al. spectroscopic LF is not corrected for completeness in the faint bins. For the purposes of comparison, all points have been converted to the same cosmology and shifted to 24 μm (when necessary) using an assumed continuum shape of −0.5. The reader is directed to the plot for the key.
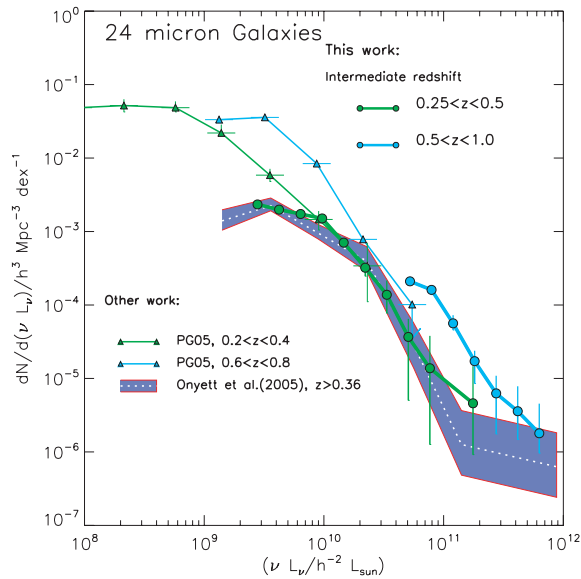

Figure 13. Comparison of 24-μm galaxy LF to similar work: intermediate redshift. Similar to Fig. 12, now for intermediate redshifts.

works, whilst, crucially, extending the LFs to high luminosity at high redshift where the results show continued evolution.

Comparison to GALFORM+GRASIL

Finally, we compare our 3.6- and 24-μm galaxy LFs to model predictions from (Lacey et al. 2005; Lacey et al., in preparation) that com-
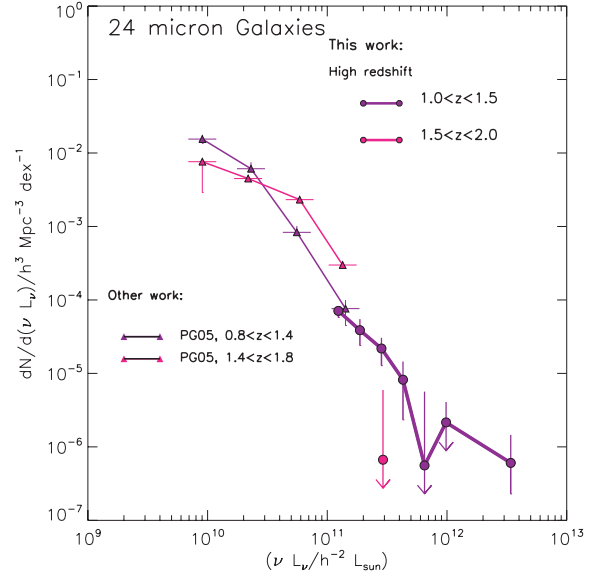

Figure 14. Comparison of 24-μm galaxy LF to similar work: high redshift. Similar to Fig. 12, now for high redshifts.

bine output from a semi-analytic galaxy formation model (GAL-FORM, Baugh et al. 2005; Cole et al. 2000), with the GRASIL spectrophotometric code (Silva et al. 1998; Granato et al. 2000). This GALFORM+GRASIL model first calculates the mass assembly and star formation histories of galaxies in the framework of the Lambda cold dark matter (ΛCDM) cosmology, and then computes self-consistent luminosities for each galaxy, from the FUV to the submm, from which LFs can be readily calculated.

In Figs 15 and 16, we compare our 3.6- and 24-μm galaxy LFs to two models which differ only in the initial mass function (IMF)
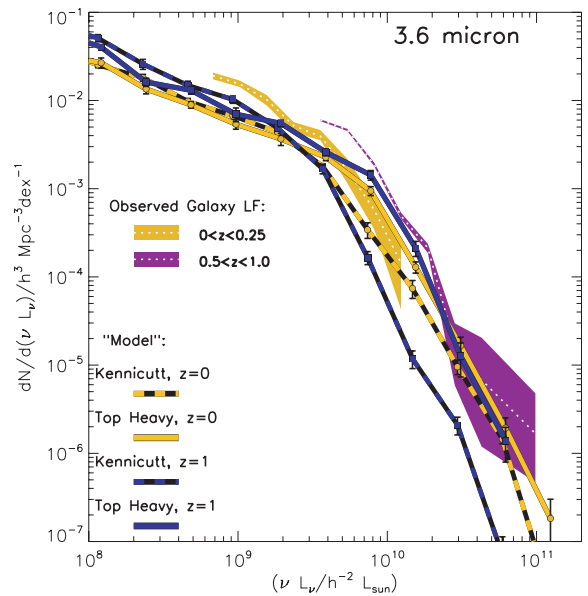

Figure 15. Comparison of 3.6-μm galaxy LF to model. The shaded regions are the observed galaxy LF at $0 < z < 0.25$ (orange) and $0.5 < z < 1$ (lilac), with the dotted line marking the LF and the region representing the 1σ errors. Overplotted are the models of Lacey et al. for the redshifts 0 (orange) and 1 (blue) split into Kennicutt (1983) and top-heavy IMF versions as striped and solid lines, respectively.
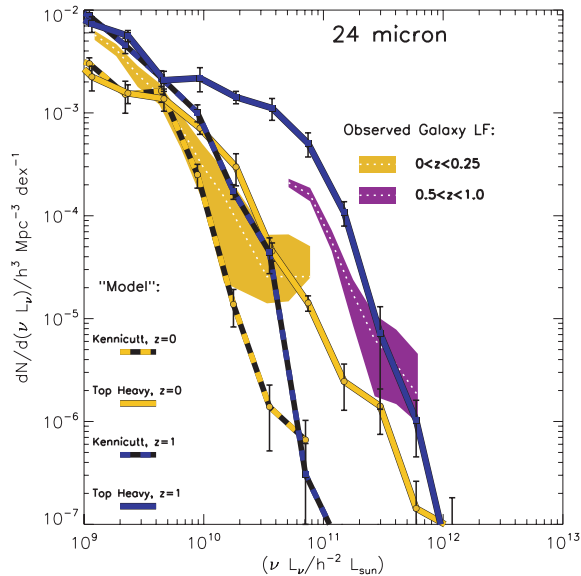
Figure 16. Comparison of 24-μm galaxy LF to model. The shaded regions are the observed galaxy LF at $0 < z < 0.25$ (orange) and $0.5 < z < 1$ (lilac), with the dotted line marking the LF and the region representing the 1σ errors. Overplotted are the models of Lacey et al. for the redshifts 0 (orange) and 1 (blue) split into Kennicutt (1983) and top-heavy IMF versions as striped and solid lines, respectively.
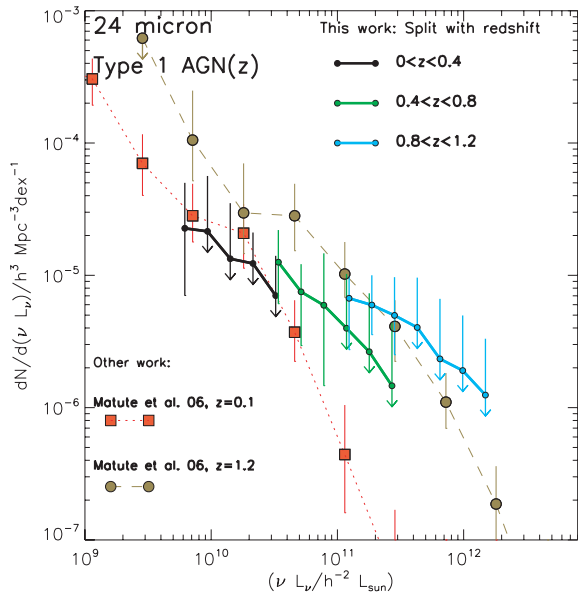

Figure 17. Comparison of 24-μm Type 1 AGN LF to similar works. Comparison to the 15-μm ELAIS AGN LF of Matute et al. (2006). For the purposes of comparison all points have been converted to the same cosmology and shifted to 24 μm using an assumed continuum shape of −0.5.

assumed. In one model, labelled 'Kennicutt' in the figures, all stars form with a solar neighbourhood IMF (we use the Kennicutt 1983 parametrization, which is close to Salpeter above $1\,M_{\odot}$, but with a flatter slope below this), while in the other model, labelled 'top-heavy', stars formed in bursts triggered by galaxy mergers are assumed to have a top-heavy IMF, with a much larger fraction of high-mass stars than in the solar neighbourhood. The parameters of the 'top-heavy' model are identical to those used in (Baugh et al. 2005),
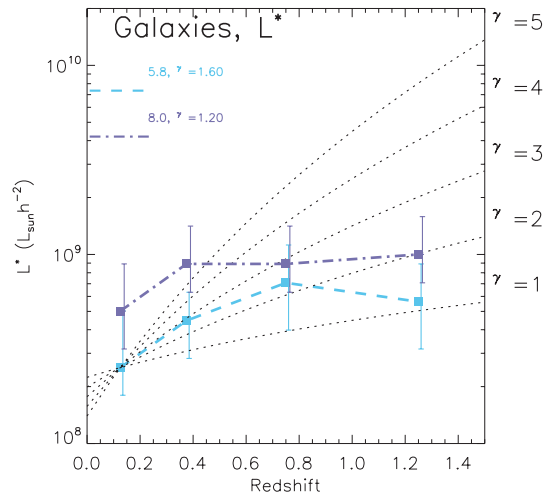

Figure 18. L^* ($L_{\odot}\,h^{-2}$) for 5.8- and 8-μm galaxies. 5.8- and 8-μm parameters result from PLE power-law fits. The overlaid dotted lines, renormalized to the 5.8-μm value in the first redshift bin, show the trend if $L^*\Phi^* \propto (1+z)^{\gamma}$, for various γ. The best-fitting γ are $\gamma = 1.6^{+0.7}_{-0.6}$ at 5.8 μm and $\gamma = 1.2^{+0.4}_{-0.5}$ at 8 μm (1σ errors in the parameter space).

who found that a top-heavy IMF was essential for their CDM-based model to reproduce the observed numbers of faint submm galaxies, and have not been adjusted to match the data from *Spitzer*. It can be seen that the IMF models diverge at high luminosity and redshift, where the top-heavy IMF produces more sources of high luminosity. This is most apparent at 24 μm, where more UV photons from the most massive stars are reradiated by dust but even at 3.6 μm there is a clear increase for the top-heavy IMF since more high-mass stars evolve though the Asymptotic Giant phase. We see that at both 3.6 and 24 μm, our measured LFs are consistent with the model LFs based on a top-heavy IMF, and lie some distance from the predictions for a standard IMF, which in particular underestimate the number of luminous galaxies, especially at higher redshift.

This is a very interesting result. While our measurements of the LF cannot uniquely determine the form of the IMF, it does seem that, when combined with galaxy formation models, the observed evolution in the LF at both 3.6 and 24 μm favours an IMF in starbursts which is skewed towards higher masses compared to the solar neighbourhood. Such a top-heavy IMF is also suggested by observations of chemical abundances in elliptical galaxies and the intracluster gas in galaxy clusters, which seem to require larger yields of heavy elements than are predicted for a standard IMF (Nagashima et al. 2005a,b). A top-heavy IMF would also help significantly in reconciling theoretical models of galaxy formation based on CDM with results from extragalactic submm surveys. The large numbers of distant IR-luminous sources found by SCUBA (Eales et al. 1999; Scott et al. 2002; Borys et al. 2003) pose a significant challenge to CDM-based models, and early versions struggled to explain both the observed submm counts, and the inferred SFRs in these sources (e.g. Granato et al. 2000). Later models have therefore invoked a variety of solutions to this problem, including a top-heavy stellar IMF, as proposed by Baugh et al. (2005); in this way, the same submm flux can be generated with substantially lower SFRs. Our results lend further observational support to this idea which, if true, means that the colossal SFRs (up to several thousand $M_{\odot}$ per year) currently inferred for distant submm sources may need to be revised significantly downwards, possibly to levels comparable to those seen in

local ultraluminous infrared galaxies (ULIRGs) (e.g. Farrah et al. 2003).

6.2 Quasars

The evolution of quasars is well established. Most studies agree that the space density of quasars above a given luminosity increases by a large factor ($\sim$50) out to $z \sim 2$, then levels out, and then decreases to $z \sim 5$ (e.g. Croom et al. 2004; Richards et al. 2006). The decrease from redshift $z \sim 2$ to the present day can be interpreted as due to a reduction in the merger rate, a decrease in the cold gas available for fuelling and an increase in the time-scale of gas accretion (Kauffmann & Haehnelt 2000).

In this work, we see a strong increase in the space density at a given luminosity from the $0 < z < 1$ to the $1 < z < 2$ bin for all bands and further increase in the $2 < z < 3$ bin. At higher redshift, the number statistics become poorer but are consistent with a constant/rising space density. The recent 8-μm Type 1 quasar evolution of Brown et al. (2006), derived from $S(24\,\mu m) > 1$ mJy sources with $1 < z < 5$, found the peak quasar space density to be at $z = 2.6 \pm 0.3$, whilst here the 8-μm luminosity evolution shown in Fig. 19 rises strongly to $2 < z < 3$ and then flattens off.

Hence, our broad-brush photometric redshift approach finds a similar result to other quasar studies whilst extending the Type 1 AGN LFs to the *Spitzer* wavebands. However, due to the depth of the SWIRE Survey, we are unable to fully observe the onset of strong decline at the highest redshifts. From optical studies this strong decline in Type 1 AGN activity occurs above redshifts of $\sim$3–4, which is our highest redshift bin, and has been seen in numerous quasar studies since the early 80s (e.g. Osmer 1982; Warren, Hewett & Osmer 1994; Kennefick, Djorgovski & de Carvalho 1995; Schmidt, Schneider & Gunn 1995; Fan et al. 2001). This dramatic drop can be interpreted as marking the epoch of peak formation of quasars, at around 10 per cent of the current age of the Universe. As such, it has strong implications for models of black hole formation, fuelling and evolution (e.g. Haehnelt & Rees 1993; Granato et al. 2001; Hatziminaoglou et al. 2003; Borys et al. 2005).
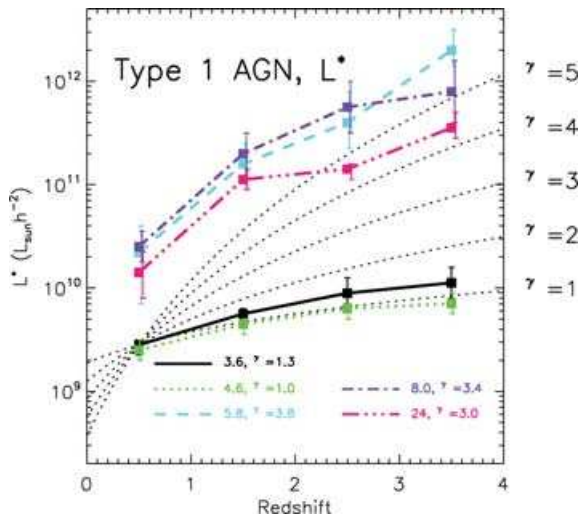

Figure 19. L^* ($L_\odot\,h^{-2}$) for Type 1 AGN. L^* values result from PLE power-law fits. The overlaid dotted lines, renormalized to the 3.6-μm value in the first redshift bin, show the trend if $L^* \propto (1 + z)^\gamma$, for various γ. The best-fitting γ are, respectively, $\gamma = 1.3^{+0.1}_{-0.1}, 1.0^{+0.1}_{-0.1}, 3.8^{+0.4}_{-0.3}, 3.4^{+0.4}_{-0.3}, 3.0^{+0.5}_{-0.4}$ (1σ errors in the parameter space).

In Fig. 17, the 24-μm Type 1 AGN LF is compared to the 15-μm ELAIS AGN LF of Matute et al. (2006) (consistent with the earlier LF of Matute et al. 2002). The Matute et al. LF is split into a $z = 0.1$ population and a $z = 1.2$ population, which trace a similar behaviour to the evolution with redshift found in this work. The broad redshift bins of this work make a direct comparison problematic since wider redshift ranges have the effect of flattening the resulting LF, however, the results are consistent. For closer comparison, the LF from this work has been rebinned into narrower redshift intervals, though the resulting low numbers of 24-μm Type 1 AGN in the bins does result in upper limits, particularly at higher luminosity and for the lowest redshift bin ($z < 0.4$).

7 LUMINOSITY EVOLUTION, ENERGY AND SFR DENSITY

7.1 Schecter and double power-law fits

The LFs calculated here demonstrate the evolution of both galaxies and Type 1 AGN with redshift. We now model these LFs using Schecter Functions (Schechter 1976) and double power-law fits. The Schecter parametrization is often applied to UV/optical galaxy LFs, whilst double power-law fits have been found to be a good fit to the local IR population (e.g. Lawrence et al. 1986; Saunders et al. 1990; Takeuchi, Yoshikawa & Ishii 2003). This can be broadly explained since star formation acts as a power law in the LF and stellar mass acts as an exponential drop-off–a LF can then be seen as a convolution of the two regimes, weighted by the relative dominance of each (determined by the rest-frame wavelength).

The Type 1 AGN LF is often modelled by a double power law (Boyle, Shanks & Peterson 1988). For example, Pei (1995) used a double power-law model where the bright and faint ends were independent of redshift, with the break occurring at a luminosity that was dependent on redshift.

The Schecter parametrization is as follows.

$$\Phi(L)\,dL/L^* = \Phi^*\left(\frac{L}{L^*}\right)^\alpha e^{-L/L^*}\,dL/L^*, \tag{10}$$

whilst the double power law is described by

$$\Phi(L)\,dL/L^* = \Phi^*\left(\frac{L}{L^*}\right)^{1-\alpha}\,dL/L^*, \quad L < L^* \tag{11}$$

and

$$\Phi(L)\,dL/L^* = \Phi^*\left(\frac{L}{L^*}\right)^{1-\beta}\,dL/L^*, \quad L > L^*. \tag{12}$$

Our approach to fitting the LFs is determined by the wavelength under consideration and the extent to which the data can break parameter degeneracies. Thus, we choose to split the analyses in the following manner.

7.2 5.8- and 8-μm galaxies, and Type 1 AGN LFs – luminosity evolution

Double power-law functions are fit to the 5.8- and 8-μm galaxy LFs and to the Type 1 AGN LFs (note that Schecter fits were attempted for the 5.8-μm galaxy LF but these did not give good results, most obviously at the bright end). However, the luminosity ranges sampled by these SWIRE LFs do not allow us to constrain the faint-end well (and hence the faint-end slope and the break where the bright-end slope takes over). Thus, noting that the bright-end slopes are well described by the same slope across the redshift bins, we choose

to explore the evolution of L^* only, by fixing α, β and Φ^*. We set the faint-end slope to $\alpha = 1.3$ (cf. PG05's slope of 1–1.3 for their 24-μm sample; Zheng et al. 2006's value of 1.2 ± 0.3 from analysis of the 24-μm LFs of Le Floc'h et al. 2005 and the local value for 60-μm *IRAS* galaxies of 1.23 from Takeuchi et al. 2003 and 1.09 from Saunders et al. 1990). The bright-end slope for the 5.8- and 8-μm galaxy LFs are set by the slope in the lowest redshift bin ($0 < z < 0.25$) where it is best-constrained, giving $\beta = 2.5$ and 2.6, respectively. For the Type 1 AGN LFs a shallower slope of $\beta = 2.2$ is able to give a good fit across all the bands. The density parameter Φ^* is set to 5E-2 h^3 dex^{-1} Mpc^{-3} for the 5.8- and 8-μm galaxy LFs and to 5E-5 for the Type 1 AGN. It is important to note that although we have chosen reasonable values, for the purposes of exploring PLE the exact choice of the fixed α and Φ^* values only effects the overall scaling of L^*, not its evolution as seen by SWIRE. The resulting PLE trends are then characterized by

$$L^* \propto (1+z)^\gamma. \tag{13}$$

Fig. 18 shows the evolution of L^* for the 5.8- and 8-μm galaxies, whilst Fig. 19 shows the evolution for the Type 1 AGN. For the two galaxy LFs, L^* is seen to increase out to the $0.5 < z < 1$ redshift bin, and then flattens off at higher redshift. The best-fitting γ is found to be $\gamma = 1.6^{+0.7}_{-0.6}$ at 5.8 μm and $\gamma = 1.2^{+0.4}_{-0.5}$ at 8 μm, with the majority of the evolution occurring since $z \sim 1$. In contrast, the Type 1 AGN show positive evolution in all bands, out to the highest redshifts ($3 < z < 4$). There is a notably higher relative luminosity across redshift for $\lambda > 5$ μm in comparison to $\lambda < 5$ μm. The best-fitting γs are $\gamma = 1.3^{+0.1}_{-0.1}$ at 3.6 μm, $\gamma = 1.0^{+0.1}_{-0.1}$ at 4.5 μm, $\gamma = 3.8^{+0.4}_{-0.3}$ at 5.8 μm, $\gamma = 3.4^{+0.4}_{-0.3}$ at 8 μm and $\gamma = 3.0^{+0.5}_{-0.4}$ at 24 μm. The strong evolution at longer wavelengths is consistent with other studies–e.g. Matute et al. (2006) found a PLE model with $L \propto (1+z)^{\sim 2.9}$ was a good fit to their 15-μm ELAIS AGN LF.

7.3 3.6- and 4.5-μm galaxies – energy density

We choose to fit Schecter functions to the IRAC 3.6- and 4.5-μm galaxy LFs. As the data are sufficient to constrain the parameter space, we allow α, Φ^* and L^* to vary, except for the $1 < z < 1.5$ bin, where we use the α value fit to the $0.5 < z < 1$ slope due to the reduced data at this high redshift. We are then able to integrate the resulting Schecter functions over luminosity in order to determine the total energy density, Ω, provided by 3.6- and 4.5-μm galaxies at each redshift. This integral is plotted in Fig. 20, showing the contribution from the observed data, and from the Schecter-fits extrapolated to luminosities not sampled by the observed LFs. Consider that an old passively evolving population is characterized by PLE, dimming more quickly than a no-evolution model in the *K* band, say (e.g. de Propris et al. 1999; Ellis & Jones 2004). This scenario is essentially what is found for IRAC 3.6 and 4.5 μm, which probe the older stellar populations (indeed a PLE Schecter fit describes the change with redshift almost as well as one in which both L^* and Φ^* are allowed to vary). Fig. 20 shows that for both bands, the energy density gradually increases out to $z \sim 0.5$–1 but flattens, or even declines, at higher redshift.

7.4 24-μm galaxies – energy and SFR density

For the 24-μm galaxies, we choose to fit a double power law. Again, the data are not able to constrain the faint-end slope and the turnover and we fix the faint-end slope to $\alpha = 1.3$ and $\Phi^* = $ 5E-2 h^3 dex^{-1} Mpc^{-3} (as before in Section 7.2). However, as shown in Section 6.1, the agreement with the PG05 LF (which is at fainter luminosities)
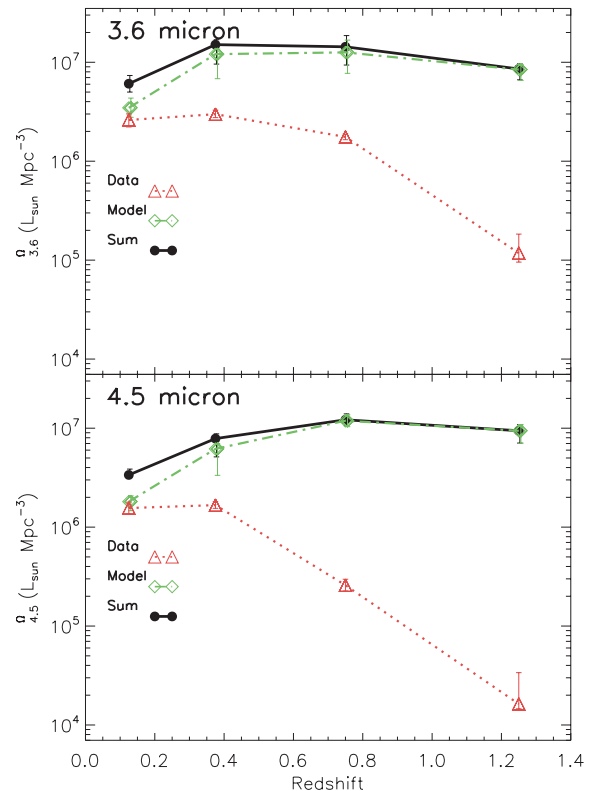

Figure 20. Integrated energy density Ω (L$_\odot$ Mpc^{-3}) for 3.6- and 4.5-μm galaxies. $\Omega_{3.6}$ and $\Omega_{4.5}$ (black circles) result from the combination of the observed data (red triangles) and the integrated Schecter-fits outside of the luminosity range where there were data (green diamonds).

is good and this choice of α and Φ^* gives double power-law fits to our data that also match well with the PG05 data at the faint-end and turnover location. This gives us confidence in extending the analysis to calculate the 24-μm energy density, Ω_{24}, by summing the contribution of our data and the integral of the double power law outside of the luminosity range in which we have data (as in Section 7.3). For the 24-μm analysis, we now go further and use Ω_{24} to obtain an estimate of the total (8–1000 μm) IR energy density, Ω_{IR} and the resulting implied cosmic-SFR density.

Total IR luminosity

The correlation between rest frame 12–15 μm and total IR luminosity for local IR-luminous galaxies has been demonstrated numerous times (e.g. Chary & Elbaz 2001; Papovich & Bell 2002) to be good, with a scatter of around 0.15 dex. Bell et al. (2005) calculated a conversion from observed-frame 24 μm to total IR luminosity using the full range of model template spectra of Dale et al. (2001), with a mean correction factor of, to within 20 per cent,

$$L_{IR} \sim 10\nu \mathrm{Ł}_\nu \,(24\,\mu\mathrm{m}). \tag{14}$$

The mean template spread around this mean was larger, ~ 0.3 dex. Similar results have been found by the study of Chary & Elbaz (2001) for *ISO* and *IRAS* galaxies, and by Le Floc'h et al. (2005) (see their fig. 8). Thus, we convert our Ω_{24} to Ω_{IR} using equation (14), which should be accurate to a factor of 2 or so (Bell et al. 2005).

SFR density

We use Ω_{IR} to obtain the SFR density using the relation of Kennicutt (1998):

$$\text{SFR}(M_\odot\ \text{yr}^{-1}) = 1.71 \times 10^{-10} L_{IR}(L_\odot). \tag{15}$$

As discussed in PG05, this conversion results in further uncertainty– the SFRs are subject to photometric redshift uncertainties, differences between different model templates and the validity of extrapolating low-redshift relationships such as that of equation (14) to higher redshift. Thus, the resulting SFRs can be expected to be subject to an additional systematic error of up to a factor of 2–3.

The cosmic IR energy density, Ω_{IR} (left-hand axis) and SFR density (right-hand axis) are plotted in Fig. 21, showing the contribution from the observed data, and from the two-power fits extrapolated to luminosities not sampled by the observed 24-μm LF. For clarity, the additional systematic uncertainties resulting from using equations (14) and (15) for conversion are not included in the plot. In contrast to IRAC, strong positive evolution, characterized by $\Omega_{IR} \propto (1 + z)^\gamma$ with $\gamma = 4.5^{+0.7}_{-0.6}$, is seen for the 24-μm galaxies, with the majority of this evolution occurring since $z \sim 1$. For comparison, Ω_{IR} results from PG05 and Le Floc'h et al. (2005) are also plotted, showing the same strong evolution. The evolution in SFR density PG05 measured was $\propto (1 + z)^{4.0 \pm 0.2}$ out to a redshift of 0.8, consistent with the evolution found in this work, and with the evolution of $\gamma = 3.9^{+0.4}_{-0.4}$ to $z \sim 1$, found by Le Floc'h et al. (2005) for their 24-μm-selected sample.

Note that parameter fit values with redshift resulting from Section 7 are given in Appendix A.

8 DISCUSSION AND CONCLUSIONS

This paper has extended the photometric redshift method to incorporate near-IR data (sub 5 μm) in the solution, improving both
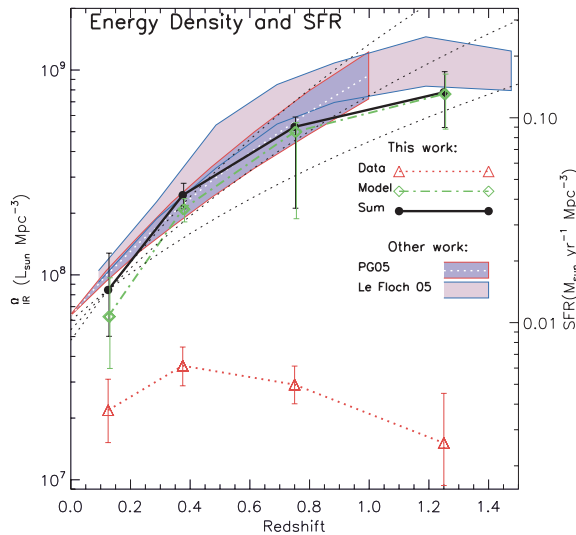

Figure 21. Integrated IR energy density Ω_{IR} and SFR density from 24-μm galaxies. Ω_{IR} (black circles) results from the combination of the observed data (red triangles) and the integrated two-power fits outside of the luminosity range where there were data (green diamonds) to obtain Ω_{24}. This is then converted to Ω_{IR} ($L_\odot$ Mpc^{-3}) and SFR ($M_\odot$ yr^{-1} Mpc^{-3}) as detailed in the text. The overlaid black dotted lines, renormalized to the value in the first redshift bin, show the best-fitting trend and 1σ spread if $\Omega_{IR} \propto (1 + z)^\gamma$, with best-fitting $\gamma = 4.5^{+0.7}_{-0.6}$. For comparison, the Ω_{IR} results from PG05 and Le Floc'h et al. (2005) are also plotted.

the accuracy and reliability of the solutions. Application of the extended photometric redshift technique to a 6.5 square degree area in the ELAIS-N1 field of the SWIRE Survey has shown that the majority of the optical SWIRE population can be characterized as star-forming galaxies with a mean redshift of $\langle z \rangle \sim 0.6$, with a tail extending out to redshifts of $z \sim 1.5$. Early-type galaxies (fit as ellipticals) make up around a fifth of the population, with a mean redshift of $\langle z \rangle \sim 0.4$ and a tail to a redshift of around unity. The proportion of 24-μm sources that are early type is seen to be lower than that of the shorter wavelength *Spitzer* sources, however, the results suggest that the frequency of dusty early types is higher than pre-*Spitzer* studies have found. Some of these sources could in fact be heavily obscured Arp220-like objects. In addition to the galaxies, there is a population of optical Type 1 AGN ($\sim$8 per cent of the total) that extends across the full redshift range, with indication of a slight rise in their distribution to redshift two to three, and a decline thereafter.

Using the photometric redshift solutions, along with selection functions designed to account for the bias in the multiwavelength catalogue, allowed LFs to be calculated in each *Spitzer* band, for both galaxies and quasars. The relevant K-corrections in the optical and IR were derived using the optical/near-IR template solutions of the redshift-fitting procedure, and separate mid-IR template-fitting solutions applied to the longer *Spitzer* wavebands. Importantly, this SWIRE sample has enabled a joint analysis of galaxy and Type 1 AGN LFs using the same sample, selection and method for both populations.

The 3.6- and 4.5-μm galaxy LFs, where the LF is probing the stellar mass, showed overall evolution consistent with the passive ageing of the dominant stellar population up to $z \sim 1.5$. The comoving luminosity density was found to evolve passively, gradually increasing out to $z \sim 0.5$–1 but flattening, or even declining, at higher redshift. Analysis with template type does, however, offer tantalizing support for 'downsizing' with starbursts showing little evolution at high luminosity and more marked evolution at lower luminosity, as would be expected if less massive/luminous galaxies remained active to later epochs.

More pronounced evolution was seen at the longest wavelength; the 24-μm galaxy LF, more indicative of SFR and/or AGN activity, undergoes strong positive evolution, with the derived IR energy density and SFR density $\propto (1 + z)^\gamma$ with $\gamma = 4.5^{+0.7}_{-0.6}$ and the majority of this evolution occurring since $z \sim 1$. This strong evolution was in agreement with other equivalent work, however, the SWIRE LFs were uniquely able to show that this evolution continues out to high luminosities at high redshift (where many models start to differ).

In addition to other observational work, comparisons to the predictions of a combined semi-analytic and spectrophotometric code were made. While we cannot provide meaningful constraints on the exact form of the IMF preferred by our LFs, an IMF skewed towards higher mass star formation in bursts compared to locally was preferred. As a result, the currently inferred massive SFRs in distant submm sources may require substantial downwards revision.

Although the results for the optical Type 1 AGN LFs are subject to greater uncertainty due to reduced photometric redshift accuracy and smaller population size, the analysis was able to demonstrate clear positive luminosity evolution in all bands, out to the highest redshifts ($3 < z < 4$). Modelling as $L^* \propto (1 + z)^\gamma$ gave $\gamma \sim 1$–1.3 for 3.6 and 4.5 μm and stronger evolution at the longer wavelengths (5.8, 8 and 24 μm), of $\gamma = 3.8^{+0.4}_{-0.3}$, $3.4^{+0.4}_{-0.3}$ and $3.0^{+0.5}_{-0.4}$, respectively.

REFERENCES

Afonso-Luis A. et al., 2004, MNRAS, 354, 961
Avni Y., Bahcall J. N., 1980, ApJ, 235, 694
Babbedge T., 2004, PhD thesis, Univ. London
Babbedge T. S. R. et al., 2004, MNRAS, 353, 654 (B04)
Babbedge T. S. R., Whitaker R., Morris S., 2005, MNRAS, 361, 437
Barger A. J., Cowie L. L., Trentham N., Fulton E., Hu E. M., Songaila A., Hall D., 1999, AJ, 117, 102
Baugh C. M., Lacey C. G., Frenk C. S., Granato G. L., Silva L., Bressan A., Benson A. J., Cole S., 2005, MNRAS, 356, 1191
Bell E. F. et al., 2005, ApJ, 625, 23
Bolzonella M., Miralles J.-M., Pelló R., 2000, A&A, 363, 476
Borys C., Chapman S., Halpern M., Scott D., 2003, MNRAS, 344, 385
Borys C., Smail I., Chapman S. C., Blain A. W., Alexander D. M., Ivison R. J., 2005, ApJ, 635, 853
Boyle B. J., Shanks T., Peterson B. A., 1988, MNRAS, 235, 935
Brown W. R., Geller M. J., Fabricant D. G., Kurtz M. J., 2001, AJ, 122, 714
Brown M. J. I. et al., 2006, ApJ, 638, 88
Bruzual A. G., Charlot S., 1993, ApJ, 405, 538
Bruzual G., Charlot S., 2003, MNRAS, 344, 1000
Bundy K., Ellis R. S., Conselice C. J., 2005, ApJ, 625, 621
Cassata P. et al., 2005, MNRAS, 357, 903
Chapman S. C., Blain A. W., Smail I., Ivison R. J., 2005, ApJ, 622, 772
Chary R., Elbaz D., 2001, ApJ, 556, 562
Chary R. et al., 2004a, ApJS, 154, 80
Chary R. et al., 2004b, ApJS, 154, 80
Chen H.-W. et al., 2003, ApJ, 586, 745
Clements D. L., Desert F. X., Franceschini A., 2001, MNRAS, 325, 665
Cohen J. G., 2002, ApJ, 567, 672
Cole S., Lacey C. G., Baugh C. M., Frenk C. S., 2000, MNRAS, 319, 168
Cole S. et al., 2001, MNRAS, 326, 255
Connolly A. J., Szalay A. S., Dickinson M., Subbarao M. U., Brunner R. J., 1997, ApJ, 486, L11
Conselice C. J. et al., 2004, ApJ, 600, L139
Cowie L. L., Songaila A., Hu E. M., Cohen J. G., 1996, AJ, 112, 839
Croom S. M., Smith R. J., Boyle B. J., Shanks T., Miller L., Outram P. J., Loaring N. S., 2004, MNRAS, 349, 1397
Dale D. A., Helou G., Contursi A., Silbermann N. A., Kolhatkar S., 2001, ApJ, 549, 215
Davoodi P. et al. 2006, MNRAS, submitted
de Jong T., Clegg P. E., Rowan-Robinson M., Soifer B. T., Habing H. J., Houck J. R., Aumann H. H., Raimond E., 1984, ApJ, 278, L67
de Propris R., Stanford S. A., Eisenhardt P. R., Dickinson M., Elston R., 1999, AJ, 118, 719
Dwek E. et al., 1998, ApJ, 508, 106
Eales S., Lilly S., Gear W., Dunne L., Bond J. R., Hammer F., Le Fèvre O., Crampton D., 1999, ApJ, 515, 518
Efstathiou A., Rowan-Robinson M., 2003, MNRAS, 343, 322
Efstathiou A., Rowan-Robinson M., Siebenmorgen R., 2000, MNRAS, 313, 734
Ellis S. C., Jones L. R., 2004, MNRAS, 348, 165
Fan X. et al., 2001, AJ, 121, 54
Farrah D., Afonso J., Efstathiou A., Rowan-Robinson M., Fox M., Clements D., 2003, MNRAS, 343, 585
Fazio G. et al., 2004, ApJS, 154, 10

Fernández-Soto A., Lanzetta K. M., Chen H., Pascarelle S. M., Yahata N., 2001, ApJS, 135, 41
Feulner G., Bender R., Drory N., Hopp U., Snigula J., Hill G. J., 2003, MNRAS, 342, 605
Fixsen D. J., Dwek E., Mather J. C., Bennett C. L., Shafer R. A., 1998, ApJ, 508, 123
Flores H. et al., 1999, ApJ, 517, 148
Fontana A. et al., 2004, A&A, 424, 23
Franceschini A., Aussel H., Cesarsky C. J., Elbaz D., Fadda D., 2001, A&A, 378, 1
Franceschini A. et al., 2005, AJ, 129, 2074 (F05)
Franceschini A. et al., 2006, preprint (astro-ph/0601003)
Girardi L., Groenewegen M. A. T., Hatziminaoglou E., da Costa L., 2005, A&A, 436, 895
Glazebrook K. et al., 2003, ApJ, 587, 55
Granato G. L., Lacey C. G., Silva L., Bressan A., Baugh C. M., Cole S., Frenk C. S., 2000, ApJ, 542, 710
Granato G. L., Silva L., Monaco P., Panuzzo P., Salucci P., De Zotti G., Danese L., 2001, MNRAS, 324, 757
Groenewegen M. A. T. et al., 2002, A&A, 392, 741
Gwyn S. D. J., Hartwick F. D. A., 1996, ApJ, 468, L77
Haehnelt M. G., Rees M. J., 1993, MNRAS, 263, 168
Hatziminaoglou E., Mathez G., Solanes J., Manrique A., Salvador-Solé E., 2003, MNRAS, 343, 692
Hatziminaoglou E. et al., 2005a, MNRAS, 364, 47
Hatziminaoglou E. et al., 2005b, AJ, 129, 1198
Hauser M. G. et al., 1998, ApJ, 508, 25
Hughes D. H. et al., 1998, Nat, 394, 241
Ibata R. A., Irwin M. J., Lewis G. F., Ferguson A. M. N., Tanvir N., 2003, MNRAS, 340, L21
Ilbert O. et al., 2004, MNRAS, 351, 541
Ilbert O. et al., 2006, preprint (astro-ph/0603217)
Irwin M., Lewis J., 2001, New Astron. Rev., 45, 105
Kauffmann G., Haehnelt M., 2000, MNRAS, 311, 576
Kennefick J. D., Djorgovski S. G., de Carvalho R. R., 1995, AJ, 110, 2553
Kennicutt R. C., 1983, ApJ, 272, 54
Kennicutt R. C., 1998, ARA&A, 36, 189
Kitsionas S., Hatziminaoglou E., Georgakakis A., Georgantopoulos I., 2005, A&A, 434, 475
Krause O., Lisenfeld U., Lemke D., Haas M., Klaas U., Stickel M., 2003, A&A, 402, L1
Lacey C. G., Baugh C. M., Frenk C. S., Granato G. L., Silva L., Bressan A., Cole S., 2005, in Proc. The Fabulous Destiny of Galaxies: Bridging Past and Present. Preprint (astro-ph/0509715)
Lagache G., Abergel A., Boulanger F., Désert F. X., Puget J. L., 1999, A&A, 344, 322
Lawrence A., Walker D., Rowan-Robinson M., Leech K. J., Penston M. V., 1986, MNRAS, 219, 687
Leeuw L. L., Sansom A. E., Robson E. I., Haas M., Kuno N., 2004, ApJ, 612, 837
Le Fèvre O. et al., 2003, The Messenger, 111, 18
Le Fèvre O. et al., 2004, A&A, 417, 839
Le Floc'h E. et al., 2005, ApJ, 632, 169
Lilly S. J., Le Fevre O., Hammer F., Crampton D., 1996, ApJ, 460, L1
Lonsdale C. J. et al., 2003, PASP, 115, 897
Lonsdale C. et al., 2004, ApJS, 154, 54
Madau P., Ferguson H. C., Dickinson M. E., Giavalisco M., Steidel C. C., Fruchter A., 1996, MNRAS, 283, 1388
Maoz D. et al., 1993, ApJ, 404, 576
Matute I. et al., 2002, MNRAS, 332, L11
Matute I., La Franca F., Pozzi F., Gruppioni C., Lari C., Zamorani G., 2006, A&A, 451, 443
McMahon R. G., Walton N. A., Irwin M. J., Lewis J. R., Bunclark P. S., Jones D. H., 2001, New Astron. Rev., 45, 97
Mobasher B., Rowan-Robinson M., Georgakakis A., Eaton N., 1996, MNRAS, 282, L7
Nagashima M., Lacey C. G., Baugh C. M., Frenk C. S., Cole S., 2005a, MNRAS, 358, 1247

Nagashima M., Lacey C. G., Okamoto T., Baugh C. M., Frenk C. S., Cole S., 2005b, MNRAS, 363, L31

Onyett N. et al., 2005, in Armus L. et al., eds, ASP Conf. Ser., Spitzer New Views Conf. Univ. Chicago Press, Chicago

Osmer P. S., 1982, ApJ, 253, 28

Papovich C., Bell E. F., 2002, ApJ, 579, L1

Papovich C., Dickinson M., Giavalisco M., Conselice C. J., Ferguson H. C., 2005, ApJ, 631, 101

Pei Y. C., 1995, ApJ, 438, 623

Pérez-González P. G. et al., 2005, ApJ, 630, 82 (PG05)

Pozzetti L. et al., 2003, A&A, 402, 837

Pozzi F. et al., 2004, ApJ, 609, 122

Puget J., Abergel A., Bernard J., Boulanger F., Burton W., Desert F., Hartmann D., 1996, A&A, 308, L5

Richards G. T. et al., 2006, AJ, 131, 2766

Rieke G. et al., 2004, ApJS, 154, 25

Rowan-Robinson M., 1995, MNRAS, 272, 737

Rowan-Robinson M., 2001, ApJ, 549, 745

Rowan-Robinson M., 2003, MNRAS, 345, 819 (RR03)

Rowan-Robinson M., Crawford J., 1989, MNRAS, 238, 523

Rowan-Robinson M., Helou G., Walker D., 1987, MNRAS, 227, 589

Rowan-Robinson M. et al., 2004, MNRAS, 351, 1290

Rowan-Robinson M. et al., 2005, AJ, 129, 1183 (RR05)

Rowan-Robinson M. et al., 2006, in Chary R.-R., ed., ASP Conf. Ser., Spitzer IR Diagnostics Conf. Univ. Chicago Press, Chicago

Saunders W., Rowan-Robinson M., Lawrence A., Efstathiou G., Kaiser N., Ellis R. S., Frenk C. S., 1990, MNRAS, 242, 318

Sawicki M. J., Lin H., Yee H. K. C., 1997, AJ, 113, 1

Schechter P., 1976, ApJ, 203, 297

Schmidt M., 1968, ApJ, 151, 393

Schmidt M., Schneider D., Gunn J., 1995, AJ, 110, 68

Scott S. E. et al., 2002, MNRAS, 331, 817

Serjeant S. et al., 2001, MNRAS, 322, 262

Serjeant S. et al., 2004, MNRAS, 355, 813

Shupe D. L., Fang F., Hacking P. B., Huchra J. P., 1998, ApJ, 501, 597

Silva L., Granato G. L., Bressan A., Danese L., 1998, ApJ, 509, 103

Surace J. et al., 2005, Technical Report, The SWIRE Data Release 2. Available at http://swire.ipac.caltech.edu/swire/astronomers/publications/SWIRE2_doc_083105.pdf

Takeuchi T., Yoshikawa K., Ishii T., 2000, ApJS, 129, 1

Takeuchi T., Yoshikawa K., Ishii T., 2003, ApJ, 587, L89

van den Bergh S., 2004, AJ, 128, 1138

Warren S. J., Hewett P., Osmer P., 1994, ApJ, 421, 412

Werner M. W. et al., 2004, ApJS, 154, 1

Willmer C. N. A., 1997, AJ, 114, 898

Xu C. K., Lonsdale C. J., Shupe D. L., Franceschini A., Martin C., Schiminovich D., 2003, ApJ, 587, 90

Zheng X. Z., Bell E. F., Rix H. W., Papovich C., Le Floc'h E., Rieke G. H., Pérez-González P. G., 2006, ApJ, 640, 784

APPENDIX A: LF FUNCTIONAL FIT PARAMETERS

Table A1. *Schecter fits*, for 3.6- and 4.5-μm galaxy LFs.

Sample	α	$L^*(\mathrm{L}_\odot\,h^{-2})$	$\Phi^*(h^3\,\mathrm{Mpc}^{-3}\,\mathrm{dex}^{-1})$	Redshift
3.6 μm	−0.9	3.6×10^{-3}	$5.6^{7.1}_{4.5} \times 10^9$	0–0.25
	−1.0	4.5×10^{-3}	$7.9^{8.9}_{7.1} \times 10^9$	0.25–0.5
	−0.9	7.0×10^{-3}	$6.8^{9.1}_{7.9} \times 10^9$	0.5–1.0
	−0.9	4.0×10^{-3}	$7.1^{7.9}_{5.6} \times 10^9$	1.0–1.5
4.5 μm	−0.9	4.5×10^{-3}	$2.8^{3.2}_{2.2} \times 10^9$	0–0.25
	−1.0	6.7×10^{-3}	$3.2^{3.5}_{2.8} \times 10^9$	0.25–0.5
	−1.1	7.7×10^{-3}	$3.2^{3.5}_{2.8} \times 10^9$	0.5–1.0
	−1.1	6.9×10^{-3}	$3.2^{3.5}_{2.5} \times 10^9$	1.0–1.5

Table A2. *L* fit parameters*, for 5.8- and 8-μm galaxy LFs. Double power law, fixed parameters are $\alpha = 1.3$, $\beta = 2.5$ (5.8 μm) and 2.6 (8 μm), $\Phi^* =$ 5E-2 h^3 dex^{-1} Mpc^{-3}. Best-fitting γ is given for $L^* \propto (1+z)^\gamma$.

Sample	$L^*(\mathrm{L}_\odot\,h^{-2})$	Redshift	γ
5.8 μm	$2.5^{4.0}_{2.2} \times 10^8$	0–0.25	$1.6^{+0.7}_{-0.6}$
	$4.5^{6.3}_{2.8} \times 10^8$	0.25–0.5	
	$7.1^{11.2}_{4.0} \times 10^8$	0.5–1.0	
	$5.6^{8.9}_{3.2} \times 10^8$	1.0–1.5	
8.0 μm	$5.0^{8.9}_{3.2} \times 10^8$	0–0.25	$1.2^{+0.4}_{-0.5}$
	$8.9^{14.1}_{6.3} \times 10^8$	0.25–0.5	
	$8.9^{14.1}_{6.3} \times 10^8$	0.5–1.0	
	$1.0^{1.6}_{0.7} \times 10^9$	1.0–1.5	

Table A3. *L* fit parameters*, for Type 1 AGN LFs. Double power law, fixed parameters are $\alpha = 1.3$, $\beta = 2.2$, $\Phi^* =$ 5E-5 h^3 dex^{-1} Mpc^{-3}. Best-fitting γ is given for $L^* \propto (1+z)^\gamma$.

Sample	$L^*(\mathrm{L}_\odot\,h^{-2})$	Redshift	γ
3.6 μm	$2.8^{3.2}_{2.2} \times 10^9$	0–1	$1.3^{+0.1}_{-0.1}$
	$5.6^{6.3}_{5.0} \times 10^9$	1–2	
	$8.9^{12.6}_{7.1} \times 10^9$	2–3	
	$1.1^{1.6}_{0.8} \times 10^{10}$	3–4	
4.5 μm	$2.5^{3.2}_{2.0} \times 10^9$	0–1	$1.0^{+0.1}_{-0.1}$
	$4.5^{5.0}_{3.6} \times 10^9$	1–2	
	$6.3^{7.1}_{5.0} \times 10^9$	2–3	
	$7.1^{8.9}_{5.6} \times 10^9$	3–4	
5.8 μm	$2.2^{4.0}_{0.7} \times 10^{10}$	0–1	$3.8^{+0.4}_{-0.3}$
	$1.6^{2.5}_{0.9} \times 10^{11}$	1–2	
	$4.0^{7.9}_{2.2} \times 10^{11}$	2–3	
	$2.0^{3.2}_{1.4} \times 10^{12}$	3–4	
8.0 μm	$2.5^{3.6}_{1.8} \times 10^{11}$	0–1	$3.4^{+0.4}_{-0.3}$
	$2.0^{3.2}_{1.1} \times 10^{11}$	1–2	
	$5.6^{10.0}_{3.2} \times 10^{11}$	2–3	
	$7.9^{1.6}_{4.0} \times 10^{11}$	3–4	
24 μm	$1.4^{2.2}_{0.8} \times 10^{10}$	0–1	$3.0^{+0.5}_{-0.4}$
	$1.1^{1.4}_{0.9} \times 10^{11}$	1–2	
	$1.4^{1.6}_{1.1} \times 10^{11}$	2–3	
	$3.6^{5.0}_{2.8} \times 10^{11}$	3–4	

Table A4. *Double power-law functional fit parameters*, for the 24-μm galaxy LF with $\alpha = 1.3$ and $\Phi^* =$ 5E-2 h^3 dex^{-1} Mpc^{-3}. Best-fitting γ is given for $L^* \propto (1+z)^\gamma$.

Sample	β	$L^*(\mathrm{L}_\odot\,h^{-2})$	Redshift	γ
24 μm	−2.5	$3.6^{6.3}_{1.8} \times 10^8$	0–0.25	$1.6^{+0.7}_{-0.6}$
	−3.0	$1.6^{1.9}_{1.3} \times 10^9$	0.25–0.5	
	−3.0	$3.2^{3.6}_{1.1} \times 10^9$	0.5–1.0	
	−3.0	$4.5^{5.6}_{3.0} \times 10^9$	1.0–1.5	

This paper has been typeset from a T$_{\rm E}$X/L$^{\rm A}$T$_{\rm E}$X file prepared by the author.